

Gasdermin D-mediated metabolic crosstalk promotes tissue repair

<https://doi.org/10.1038/s41586-024-08022-7>

Received: 28 September 2023

Accepted: 5 September 2024

Published online: 11 September 2024

 Check for updates

Zhexu Chi^{1,2,3,10}✉, Sheng Chen^{4,5,10}, Dehang Yang^{1,2,10}, Wenyu Cui⁶, Yang Lu¹, Zhen Wang¹, Mobai Li¹, Weiwei Yu^{4,5}, Jian Zhang², Yu Jiang¹, Ruya Sun¹, Qianzhou Yu¹, Tianyi Hu¹, Xiaoyang Lu¹, Qiqi Deng¹, Yidong Yang¹, Tianming Zhao¹, Mengfei Chang¹, Yuying Li⁷, Xue Zhang⁸, Min Shang⁹, Qian Xiao^{4,5}, Kefeng Ding^{4,5} & Di Wang^{1,2}✉

The establishment of an early pro-regenerative niche is crucial for tissue regeneration^{1,2}. Gasdermin D (GSDMD)-dependent pyroptosis accounts for the release of inflammatory cytokines upon various insults^{3–5}. However, little is known about its role in tissue regeneration followed by homeostatic maintenance. Here we show that macrophage GSDMD deficiency delays tissue recovery but has little effect on the local inflammatory milieu or the lytic pyroptosis process. Profiling of the metabolite secretome of hyperactivated macrophages revealed a non-canonical metabolite-secreting function of GSDMD. We further identified 11,12-epoxyeicosatrienoic acid (11,12-EET) as a bioactive, pro-healing oxylipin that is secreted from hyperactive macrophages in a GSDMD-dependent manner. Accumulation of 11,12-EET by direct supplementation or deletion of *Ephx2*, which encodes a 11,12-EET-hydrolytic enzyme, accelerated muscle regeneration. We further demonstrated that EPHX2 accumulated within aged muscle, and that consecutive 11,12-EET treatment rejuvenated aged muscle. Mechanistically, 11,12-EET amplifies fibroblast growth factor signalling by modulating liquid–liquid phase separation of fibroblast growth factors, thereby boosting the activation and proliferation of muscle stem cells. These data depict a GSDMD-guided metabolite crosstalk between macrophages and muscle stem cells that governs the repair process, which offers insights with therapeutic implications for the regeneration of injured or aged tissues.

In metazoan organisms, the regeneration process depends on the coordination of various cell types within the wound microenvironment, among which macrophages have a central role¹. The functional state of macrophages is dynamic during tissue regeneration and exerts distinct crosstalk with stroma and other immune components that are essential for a successful healing process^{2,6}. This complicated intercellular communication includes traditional protein ligand–receptor pairs, as well as small metabolites, which serve as messengers that diffuse in the wound microenvironment⁷. Although the role of macrophage-guided metabolic interplay has been proposed, how these metabolic signals are actively released into the wound-healing milieu and their potential effects on neighbouring cells are not well characterized.

Inflammation is an evolutionarily conserved process that serves to protect against harmful insults by reinforcing the defence of homeostasis and preserving the functional and structural integrity of tissues and organs⁸. As the culmination of various inflammatory cascades, cleavage of GSDMD forms membrane pores to initiate pyroptosis, which

enables the release of numerous pro-inflammatory cytokines, conferring its predominant contribution in warding off pathogen invasion and inflammatory diseases^{9,10}. In addition to its canonical role in cell death, GSDMD regulates pyroptosis-independent aspects of cellular homeostasis under different circumstances^{11–14}, but little is known about whether this non-canonical function of GSDMD participates in the tissue regeneration process. Although a few small proteins have been reported to be secreted via GSDMD pores¹⁵, the full metabolic secretome and its effects on physiological processes have not yet been defined.

GSDMD knockout compromises tissue repair

Cardiotoxin (CTX)-induced acute muscle injury is a paradigmatic self-limiting sterile injury model for exploring the tissue regeneration process¹⁶, which consists of a series of tightly regulated events, including an initial inflammatory response and the activation of muscle

¹Institute of Immunology and Sir Run Run Shaw Hospital, Zhejiang University School of Medicine, Hangzhou, China. ²Liangzhu Laboratory, Zhejiang University Medical Center, Hangzhou, China. ³Center for Regeneration and Aging Medicine, The Fourth Affiliated Hospital of School of Medicine, and International School of Medicine, International Institutes of Medicine, Yiwu, China. ⁴Department of Colorectal Surgery and Oncology (Key Laboratory of Cancer Prevention and Intervention, Ministry of Education), The Second Affiliated Hospital, Zhejiang University School of Medicine, Hangzhou, China. ⁵Center for Medical Research and Innovation in Digestive System Tumors, Ministry of Education, Hangzhou, China. ⁶Eye Center, The Second Affiliated Hospital, Zhejiang University School of Medicine, Hangzhou, China. ⁷CAS Key Laboratory of Nutrition, Metabolism and Food Safety, Shanghai Institute of Nutrition and Health, Chinese Academy of Sciences, University of Chinese Academy of Sciences, Shanghai, China. ⁸Department of Pathology and Pathophysiology, Zhejiang University School of Medicine, Hangzhou, China. ⁹Department of Cardiology, Sir Run Run Shaw Hospital, Zhejiang University School of Medicine, Hangzhou, China. ¹⁰These authors contributed equally: Zhexu Chi, Sheng Chen, Dehang Yang. ✉e-mail: ralf@zju.edu.cn; diwang@zju.edu.cn

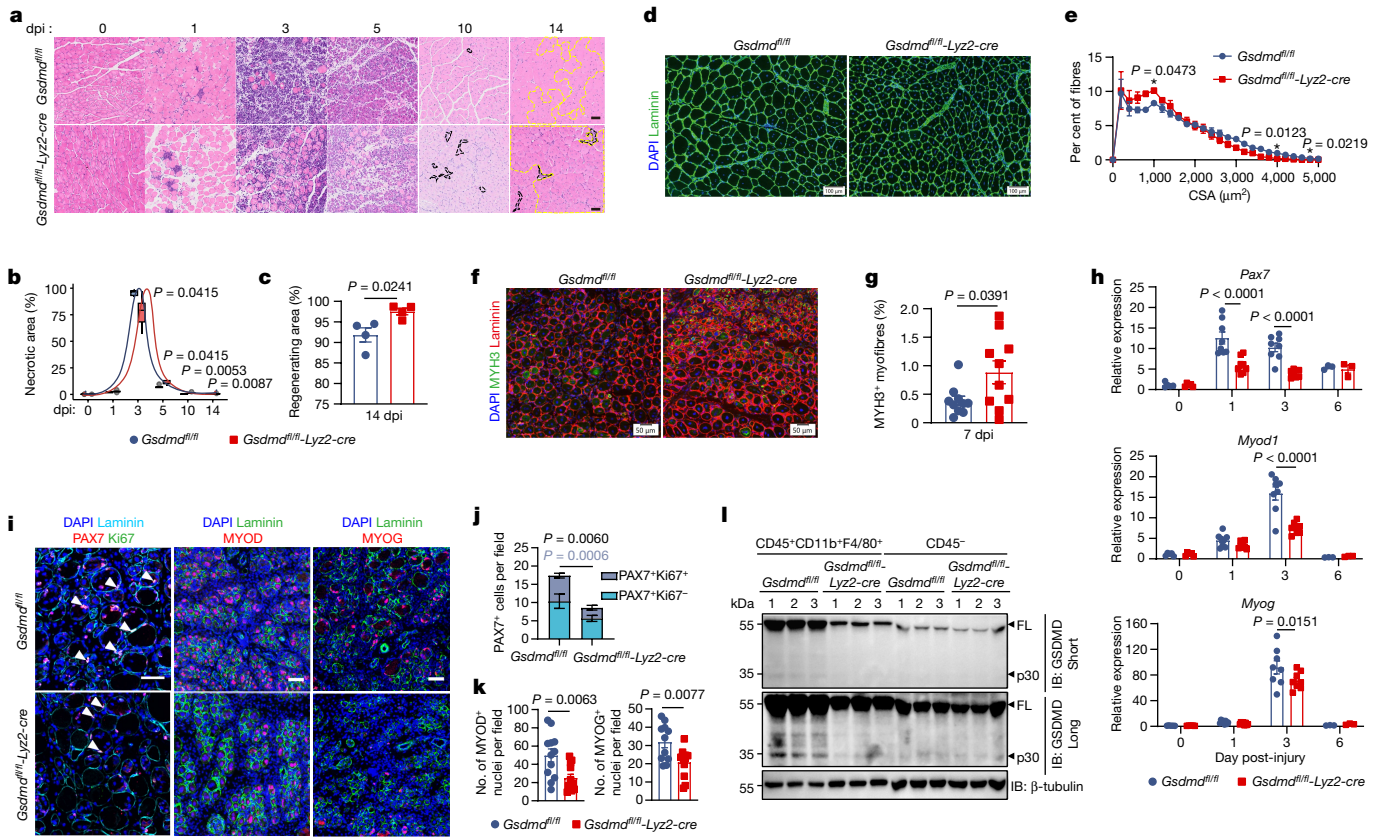


Fig. 1 | Myeloid GSDMD deficiency compromises tissue repair.

a–c, Representative haematoxylin and eosin (H&E) staining of tibialis anterior (TA) muscle cross-sections at 0, 1, 3, 5, 10 and 14 days after CTX-induced injury (**a**), the percentage of necrotic area (indicated by black dashed lines in **a**) (**b**; 0 dpi: $n = 5$ *Gsdmd*^{fl/fl}, 4 *Gsdmd*^{CKO}; 1, 3 and 10 dpi: $n = 6$; 5 dpi: $n = 5$; 14 dpi: $n = 4$) and regenerating area (yellow dashed line in **a**) at 14 dpi (**c**; $n = 4$). **d,e,** Representative TA muscle cross-sections (**d**) and the distribution of CSA (**e**; $n = 4$) at 14 dpi. **f,g,** Representative micrographs (**f**) and quantification ($n = 10$) (**g**) of MYH3⁺ myofibres at 7 dpi. **h,** Quantitative PCR with reverse transcription RT-qPCR analysis of *Pax7*, *Myod1* and *Myog* mRNA expression at indicated dpi (0 dpi: $n = 5$; 1 dpi: $n = 8$; 6 dpi: $n = 3$). **i–k,** Representative

immunofluorescence staining (**i**) and quantification of quiescent (PAX7⁺Ki67⁻) and proliferating (PAX7⁺Ki67⁺) MuSCs (**j**; $n = 8$) and early ($n = 12$, MYOD⁺ nuclei) and late ($n = 11$, *Gsdmd*^{fl/fl}; $n = 12$, *Gsdmd*^{CKO}, MYOG⁺ nuclei) differentiation markers (**k**) at 3 dpi. **i**, White arrows indicate PAX7⁺Ki67⁺ cells. **l,** Western blot analysis of GSDMD in sorted macrophages and CD45⁻ cells. Short and long exposures are shown. One representative (**a–f,i,l**) or a pool from at least two independent experiments (**g,h,j,k**) is shown. Unpaired two-tailed *t*-test (**c,g,j,k**); multiple two-tailed *t*-test with Holm–Šidák correction (**b**); two-way ANOVA with Šidák correction (**e,h**). Data are mean \pm s.e.m. Scale bars: 50 μm (**a,f,i**), 100 μm (**d**). In all figures, n refers to the number of muscle samples.

stem cells (MuSCs), as well as later inflammation resolution along with MuSC proliferation and differentiation¹⁷ (Extended Data Fig. 1a). To determine the role of myeloid-expressing GSDMD in tissue regeneration, we generated *Gsdmd*^{fl/fl-Lyz2-cre} (*Gsdmd*^{CKO}) mice. *Gsdmd* deficiency did not influence the number of MuSCs in the homeostatic state (Extended Data Fig. 1b), but resulted in a delayed repair process, evidenced by persistence of the necrotic area and regenerating area within regenerating muscles (Fig. 1a–c), as well as a reduction in the cross-sectional area (CSA) of new myofibres (Fig. 1d,e and Extended Data Fig. 1c) at the late stage of regeneration. Consistently, muscles from *Gsdmd*^{CKO} mice contained more early-regenerating myofibres (positive for myosin-3 (MYH3, also known as eMyHC)) at 7 days post-injury (dpi) (Fig. 1f,g), indicating a blunted muscle healing process. The regeneration process was similar between *Gsdmd*^{fl/fl} and *Gsdmd*^{CKO} mice upon macrophage depletion (Extended Data Fig. 1d,e), in terms of muscle strength (Extended Data Fig. 1f) and CSA of new myofibres (Extended Data Fig. 1g–i). These data indicated that the pro-regenerative effect of GSDMD during muscle damage relies largely on intramuscular macrophage populations.

The regeneration of muscle following injury relies on the activation of quiescent MuSCs to upregulate programs of myogenic activity^{17,18}, with consecutive expression of *Pax7*, *Myod1* (also known as *MyoD*) and *Myog* (Extended Data Fig. 1j). In line with the delayed regeneration

phenotypes, *Gsdmd*^{CKO} mice showed decreased mRNA levels of these gene programs (Fig. 1h). Upon activation, MuSCs first undergo robust proliferation, followed by exit from the cell cycle to either differentiate and subsequently fuse to repair damaged myofibres or return to the quiescent state^{16–19}. Accordingly, immunofluorescence staining showed significantly attenuated proliferation of *Gsdmd*^{CKO} MuSCs (Fig. 1i,j), with sequential decreased differentiation levels (Fig. 1i,k). To determine the functional relevance of GSDMD and MuSC activation, we examined the cleavage of GSDMD, and found that cleaved N-terminal GSDMD (p30) appeared at 1 dpi, and peaked at 3 dpi (Extended Data Fig. 1k,l), coinciding with macrophage infiltration (Extended Data Fig. 1m). We further confirmed that this GSDMD cleavage occurred predominantly in intramuscular macrophages (Fig. 1l). Consistently, macrophage depletion significantly diminished the amount of cleaved GSDMD in total muscle lysates (Extended Data Fig. 1n). Additionally, GSDMD deficiency did not influence the acute infiltration of macrophages during the early stage of regeneration (0–3 dpi), and maintained macrophage infiltration until 10 dpi (Extended Data Fig. 1m). Alteration of blood vessels is crucial for tissue regeneration²⁰; we found that loss of GSDMD did not alter vascular density (Extended Data Fig. 1o). Collectively, these data indicated that GSDMD is required for optimal muscle repair, but had little effect on the establishment of an early inflammatory niche upon injury.

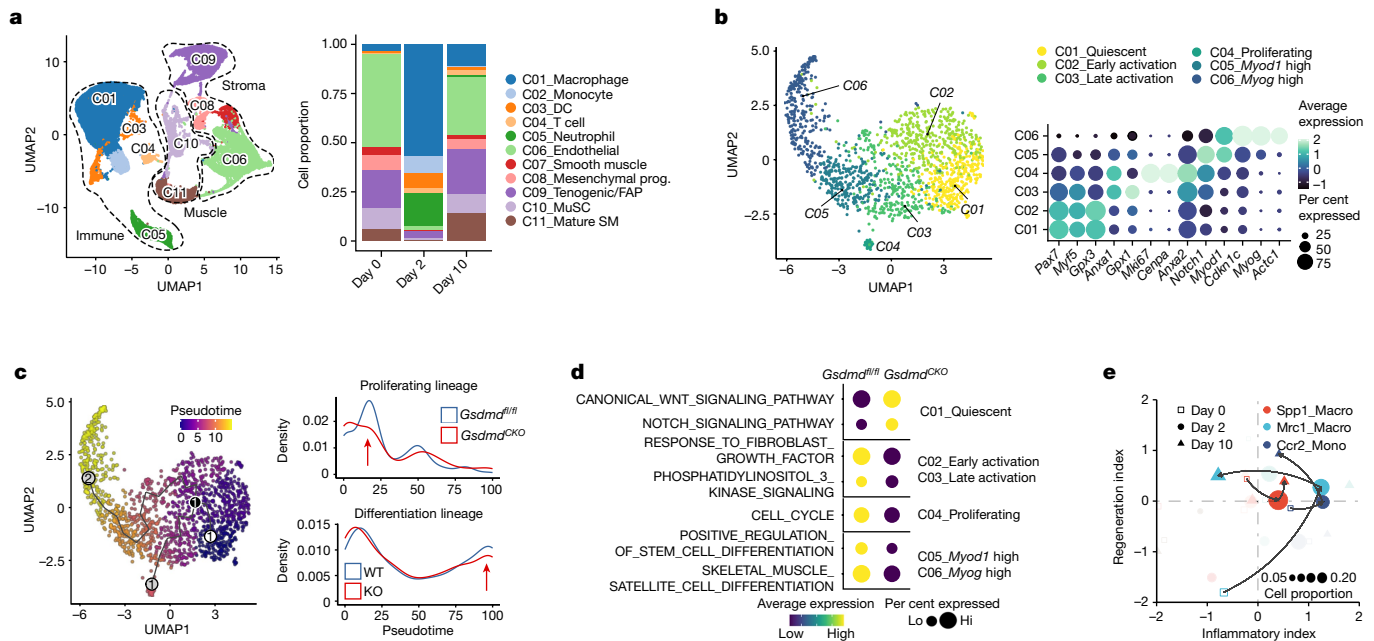


Fig. 2 | Myeloid-expressing GSDMD is essential for MuSC function during regeneration. **a**, Total cells from muscle tissue were loaded for single-cell sequencing. Uniform manifold approximation and projection (UMAP) plot of integrated cell clustering and changes of cell proportion during regeneration. DC, dendritic cell; FAP, fibro-adipogenic progenitor; prog., progenitor; SM, smooth muscle. **b**, Left, UMAP analysis of six consecutive MuSC subpopulations. Right, dot plot of relative expression of marker genes. **c**, Trajectory analysis

of the MuSC lineage (left) and density plots of the relative number of MuSCs (right). Red arrow indicates the disordered proliferation lineage (right, top) and fewer terminally differentiated *Myog*^{hi} MuSCs (right, bottom) in *Gsdmd*^{CKO} mice. **d**, Dot plot of the enrichment scores of indicated gene sets calculated by the AddModuleScore function. FGF, fibroblast growth factor. **e**, VISION-based enrichment analysis to evaluate the functional states of each immune cell type. The plot shows the dynamics of each immune cell type during tissue repair.

GSDMD is essential for MuSC function

Successful tissue repair requires various cell types within muscle to act in a sequential and coordinated cascade to initiate stem cell activation, clear damaged debris, resolve inflammation and re-establish homeostasis¹⁶. To identify the full spectrum of muscle regeneration processes upon GSDMD deficiency, we collected muscle tissue at early (day 2) and late (day 10) stages of regeneration for single-cell sequencing. After quality control, we collected a total of 51,945 cells, including 11 major cell types (Fig. 2a and Extended Data Fig. 2a–d). Upon injury, MuSCs exit the quiescent state and transit to the proliferating state in order to initiate the regeneration process²¹. We subclustered post-injury MuSCs into six sequential states, including quiescent, early activation, late activation, proliferating, *Myod1*^{high} and terminally differentiated *Myog*^{high} clusters (Fig. 2b), and further confirmed that this temporal transition of MuSCs is negatively correlated with their regenerative potential (Extended Data Fig. 2e,f). We next performed pseudotime trajectory analysis²² and identified two conserved MuSC transition states corresponding to the different fates after MuSC activation^{17,19} in *Gsdmd*^{fl/fl} versus *Gsdmd*^{CKO} mice (Fig. 2c). GSDMD deficiency led to a disordered proliferating lineage with fewer early-stage cells, and decreased differentiation towards terminal *Myog*^{high} cells (Fig. 2c). The maintenance of quiescence and the transition to the proliferating state upon injury are tightly regulated by a series of signalling cascades²³ (Extended Data Fig. 2g). We also found that MuSCs from *Gsdmd*^{CKO} mice showed persistent activation of Notch and Wnt signalling pathways (Fig. 2d), which have crucial roles in MuSC quiescence¹⁷. By contrast, GSDMD deficiency attenuated activation of PI3K-AKT and fibroblast growth factor receptor (FGFR)-MAPK signalling pathways in MuSCs, reducing the transition from quiescence to activation¹⁸, leading to decreased levels of proliferation and differentiation (Fig. 2d). Furthermore, phosphorylation of proteins in these key signalling cascades was significantly reduced in muscles lacking GSDMD (Extended Data Fig. 2h). Together, these data indicated that GSDMD is required for

efficient transitioning of MuSCs from a quiescent to a proliferating state, which is crucial for the early formation of the regenerative niche upon acute injury.

MuSC function is tightly regulated by various intramuscular cell populations²⁴. We found that GSDMD myeloid conditional knockout had little effect on the overall cell type populations. The transient expansion of intramuscular pro-inflammatory immune components at the early stage post-injury was conserved in control and *Gsdmd*^{CKO} mice (Fig. 2a and Extended Data Fig. 3a–d), indicating that *Gsdmd*^{CKO} may not directly influence the early intramuscular inflammatory niche during muscle injury.

Muscle regeneration is linked with a temporal transition from the initial inflammatory microenvironment towards the late pro-regenerative microenvironment (Extended Data Fig. 3e), which provides intercellular signalling molecules that exert modulating effects on MuSCs during different stages after injury¹⁶. To identify the immune cell types that have key roles during this highly dynamic muscle regeneration process, we applied functional analysis to each immune cell type using inflammatory (Inflammatory.Index) and pro-regenerative (Regeneration.Index) gene sets in VISION. We defined three highly dynamic myeloid populations among all immune cell types, *Spp1*^{high} macrophages, *Mrc1*^{high} macrophages and *Ccr2*^{high} monocytes (Fig. 2e and Extended Data Fig. 3f), which upregulated inflammatory programs during the acute phase post-injury (from hollow square to solid circle), while transitioning to the pro-regenerative phenotype in the late phase (from solid circle to solid triangle) (Fig. 2e). VISION-based enrichment analysis further showed that GSDMD deficiency did not affect this phenotype shift of these dynamic myeloid populations (Extended Data Fig. 3g). Furthermore, trajectory analysis showed that GSDMD deficiency did not influence the monocyte-to-macrophage differentiation process (Extended Data Fig. 3h), consistent with previous results showing that *Gsdmd* knockout did not influence total macrophage infiltration during the early stage post-injury (Extended Data Figs. 1m and 3d). Cell-cell interaction analysis showed that *Gsdmd* knockout had little effect on the

expression of the top enriched ligands in immune cells (Extended Data Fig. 3i–k), indicating that GSDMD may have little influence on intercellular interactions via known ligand–receptor pairs. Thus, single-cell sequencing analysis showed that *Gsdmd* expressed by myeloid cells may be dispensable for the temporal transition of intramuscular immune components during regeneration.

GSDMD protein was originally identified as the executor of cell pyroptosis, facilitating the secretion of various pro-inflammatory such as interleukin-1 β (IL-1 β) through pores formed by the oligomerization of its N-terminal fragment⁹. Thus, to explore whether *Gsdmd* knockout affects the pyroptosis process and the subsequent release of pro-inflammatory mediators, we conducted crosslinking experiments with bis(sulfosuccinimidyl)suberate (BS³) to examine intramuscular GSDMD oligomerization during injury, and found notable N-terminal fragment oligomerization in *Gsdmd*^{f/f} mice (Extended Data Fig. 4a), indicating that GSDMD pores are formed at the early stage after muscle injury. Nevertheless, GSDMD deficiency did not influence NINJ1 oligomerization (Extended Data Fig. 4a)—a key event that leads to plasma membrane rupture upon GSDMD N-terminal fragment oligomerization^{25,26}. These data indicated that GSDMD pore formation might not be coupled with lytic pyroptosis during muscle regeneration. Moreover, given that canonical pyroptosis would lead to the robust release of pro-inflammatory mediators, we systemically analysed the intramuscular secretome using sensitive multiplex OLINK assays for key proteins involved in inflammation, regeneration and stress responses²⁷. Prior to these assays, we conducted analyses for commonly used, highly abundant, intracellular marker proteins to confirm the purity of tissue interstitial fluid (TIF) composition (Extended Data Fig. 4b).

We identified distinct early-stage versus late-stage intramuscular secretomes on the basis of principal components analysis (PCA) (Extended Data Fig. 4c), whereas GSDMD deficiency had little effect on overall interstitial fluid composition, including a series of pro-inflammatory and pro-regeneration factors. In particular, *Gsdmd* knockout did not influence interstitial levels of IL-1 β (Extended Data Fig. 4d), a key pyroptosis-releasing pro-inflammatory cytokines³. The final step of pyroptosis after GSDMD pore formation is plasma membrane rupture, which leads to passive release of large intercellular molecules²⁵. We found similar levels of HMGB1 in TIF of control and *Gsdmd*^{CKO} mice (Extended Data Fig. 4e). Moreover, on the basis of genes that are highly correlated with the pyroptosis process, we found that *Gsdmd* knockout had limited effect on the pyroptosis process of myeloid cells (Extended Data Fig. 4f), further indicating that the oligomerization of the GSDMD N-terminal fragment at the early stage of regeneration may not lead directly to lytic pyroptosis, but potentially induces a hyperactive state⁴. Together, these data reveal a pro-regenerative role of GSDMD during the early stage after injury.

11,12-EET is secreted from GSDMD pores

Considering that GSDMD may have a low pro-regenerative capacity owing to its canonical function in regulating pyroptosis-related inflammation, we established an *in vitro* conditioned medium assay to identify the crucial role of GSDMD activation in muscle regeneration. To mimic the hyperactive state of macrophages upon GSDMD activation *in vitro* without lytic pyroptosis, we supplied cells with glycine to osmoprotectively maintain plasma membrane integrity while allowing active passage through oligomerized GSDMD conduits^{3,28,29}. We next ultracentrifuged supernatants collected from control and *Gsdmd*-knockout macrophages using a 3 kDa cellulose membrane, which separated the majority of protein ligands (larger than 3 kDa) and small-molecule metabolites³⁰ (smaller than 3 kDa) (Extended Data Fig. 5a). We found that protein ligands such as IL-1 β (GSDMD-dependent), IL-6 and TNF (GSDMD-independent) were negligibly detectable in the small-molecule fraction (Extended Data Fig. 5b–d). To identify which fraction boosted muscle regeneration,

we treated mouse myoblasts with the supernatants. Of note, treatment of myoblasts with the small-molecule fraction of supernatants from *Gsdmd* wild-type macrophages resulted in greater myogenic potential than treatment with the small-molecule fraction from knockout macrophages (Fig. 3a), as indicated by increased myotube size and fusion index (Fig. 3b).

Given these results, we hypothesized that specific small molecules secreted via GSDMD pores could boost myogenesis. We used sequential treatment with lipopolysaccharide (LPS) and nigericin (LN treatment) or poly(dA:dT) (LP treatment) to trigger GSDMD cleavage and membrane pore formation⁹. We then used propidium iodide staining to label cells that formed membrane conduits, and used lactate dehydrogenase (LDH) to determine the extent of lytic cell death²⁵. To identify bona fide active (non-lytic) GSDMD-mediated secretion, we supplied cells with glycine, using *Gsdmd*^{CKO} macrophages as negative controls. As expected, glycine prevented lytic death of macrophages, with little effect on GSDMD pore formation (Extended Data Fig. 5e,f), licensing a hyperactive state of macrophages. Thus, we established a screening strategy with these two GSDMD activation models to systemically profile the secretome using untargeted metabolomics after GSDMD pore formation (Fig. 3c). Many metabolites were detected in lytic pyroptosis induced by different stimuli (Extended Data Fig. 5g). Considering that glycine supplementation would lead to the direct accumulation of glycine itself and may potentially induce other artificial signals in our screening system, we ruled out metabolites that changed significantly owing to glycine addition (Extended Data Fig. 5h). Notably, we detected one metabolite, 11,12-EET, that was consistently enriched in supernatants from hyperactive glycine-treated macrophages (Fig. 3d and Extended Data Fig. 5i) in a GSDMD-dependent manner (Extended Data Fig. 5j).

11,12-EET is an eicosanoid that is naturally converted from phospholipids³¹ (Extended Data Fig. 5k). To quantify our untargeted metabolomics result, we applied a competitive 11,12-EET ELISA assay and found that GSDMD activation led to the active secretion of 11,12-EET from hyperactive macrophages (Extended Data Fig. 5l). For further validation, we used targeted metabolomics of the eicosanoid family, and detected a total of 88 oxylipins. PCA analysis showed that GSDMD deficiency had limited influence on the intracellular composition, but led to distinct levels of the oxylipin secretome (Extended Data Fig. 5m). Consistent with the results of the untargeted metabolomics analyses, we identified several eicosanoids, including 11,12-EET, that were actively secreted in a GSDMD-dependent manner (Fig. 3e). Next, based on the calculation of the percentage of supernatant 11,12-EET relative to the total cell lysate, we further confirmed that the release of 11,12-EET, but not the total cellular amount, was significantly reduced upon GSDMD deficiency (Extended Data Fig. 5n).

Subsequently, we sought to validate these findings *in vivo*. We collected paired TIFs from muscle and muscle tissue at different time-points after CTX-induced injury. After normalizing the metabolites in TIF normalized to their levels in muscle tissue, we identified three distinct secretion patterns upon acute injury: ‘early-stage secretion’ (secreted throughout the whole early phase, 1–5 dpi), ‘transient secretion’ (secreted transiently post-injury) and ‘late-stage secretion’ (beginning at the late stage, 5 dpi) (Fig. 3f). As well as 11,12-EET, the early-phase interstitial secretome was enriched with several eicosanoid-related metabolites (Fig. 3g). We next collected TIF from *Gsdmd*^{f/f} and *Gsdmd*^{f/f-Lyz2-cre} mice and detected 11,12-EET by liquid chromatography–mass spectrometry (LC–MS/MS). Consistent with the *in vitro* data, we found that GSDMD deficiency significantly inhibited intramuscular 11,12-EET levels (Fig. 3h,i). Together, using three independent omics strategies, we identified 11,12-EET as a representative metabolite (Fig. 3j) that was actively secreted from hyperactive macrophages upon GSDMD activation.

Finally, we set out to test whether this GSDMD-dependent secretion of metabolite can directly influence muscle regeneration.

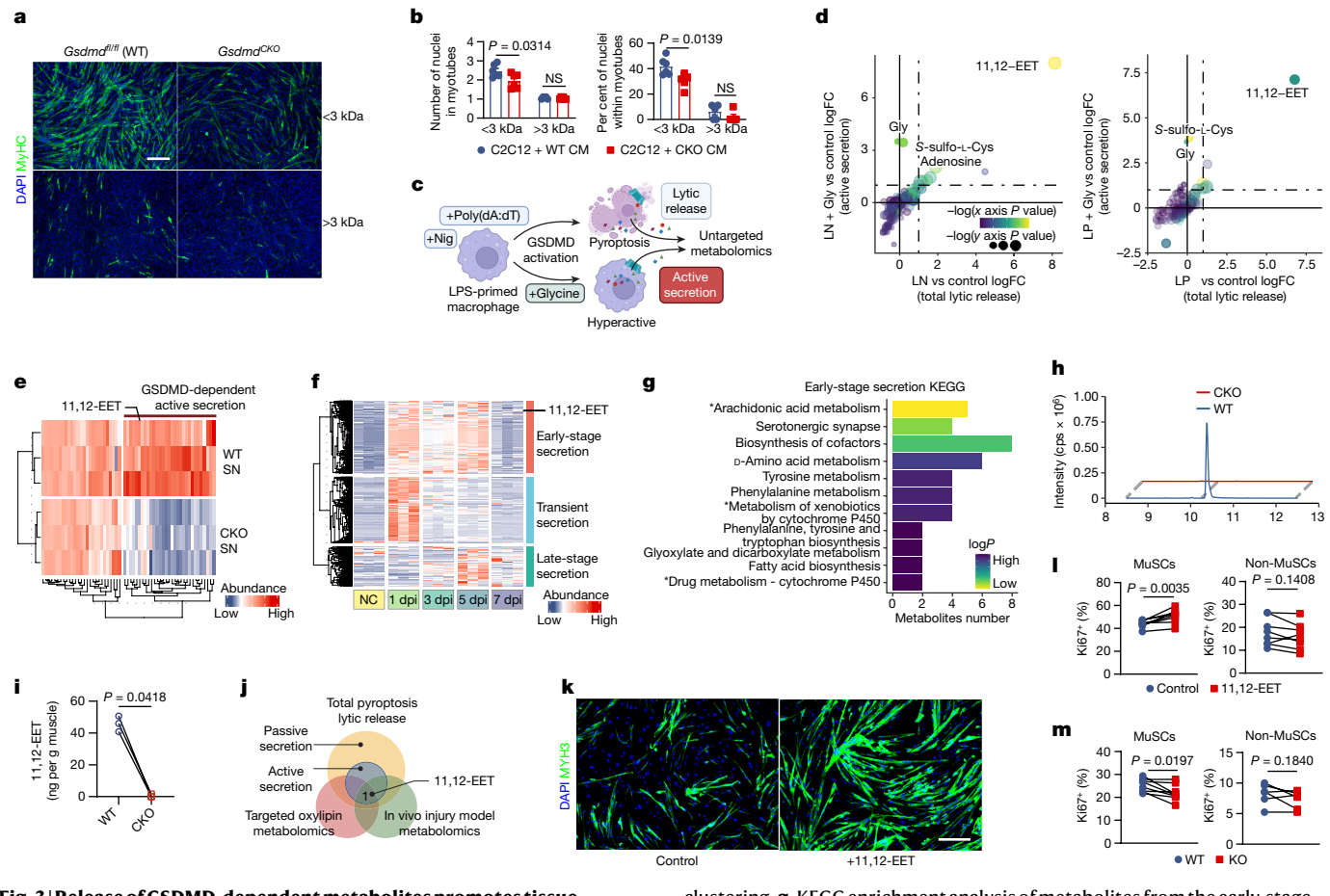


Fig. 3 | Release of GSDMD-dependent metabolites promotes tissue regeneration. **a,b**, C2C12 cells in coculture with <3 kDa and >3 kDa fractions of supernatants from hyperactivated macrophages of *Gsdmd* wild-type and knockout mice. Representative images (**a**) and quantification (**b**) of C2C12 myotube size and fusion index ($n = 6$, <3 kDa; $n = 5$, >3 kDa). NS, not significant. **c**, Schematic of the unbiased, untargeted metabolite screening strategy. Nig., nigericin. **d**, Functional correlation plot of metabolite levels in the supernatants from macrophages with the indicated treatment. FC, fold change. **e**, Metabolite levels in supernatants from hyperactivated macrophages, determined by targeted oxylipin metabolomics. **f,g**, Heat map of untargeted metabolomics of muscle TIF at different timepoints after CTX-induced injury. Three patterns of metabolite changes were determined on the basis of k-means

clustering. **g**, KEGG enrichment analysis of metabolites from the early-stage secretion pattern. **h,i**, LC-MS/MS identification (**h**) and quantification (**i**) of 11,12-EET in TIF from TA muscle ($n = 3$). **j**, Venn diagram showing significantly enriched metabolites in each experimental setting. **k**, Representative images of primary isolated MuSCs used for differentiation experiments with 11,12-EET or vehicle. **l,m**, Percentage of Ki67⁺ cells in isolated MuSCs and non-MuSCs cultured with proliferation medium supplemented with 5 μ M 11,12-EET or vehicle (**l**) or supernatants collected from *Gsdmd^{fl/fl}* and *Gsdmd^{CKO}* macrophages (**m**) for 2 days ($n = 8$, except in **m**, right, $n = 6$). A representative (**a,b,k**) or a pool (**l,m**) of at least two independent experiments is shown. Unpaired two-tailed t-test (**b**); paired two-tailed t-test (**i,l,m**). Data are mean \pm s.e.m. Scale bars, 200 μ m. cps, counts per second.

Supplementation with 11,12-EET accelerated the myogenic capacity of myoblast cell lines (Extended Data Fig. 5o,p). We also treated freshly isolated mouse MuSCs with 11,12-EET and supernatants from control and *Gsdmd*-knockout macrophages (Extended Data Fig. 5q). 11,12-EET significantly accelerated morphological changes of MuSCs upon activation (Extended Data Fig. 5r,s), boosting their myogenic potential (Fig. 3k). Furthermore, 11,12-EET (Fig. 3l and Extended Data Fig. 5t) and supernatants from control macrophages (Fig. 3m and Extended Data Fig. 5u) enhanced MuSC proliferation, and had less effect on non-MuSC cells.

11,12-EET boosts tissue regeneration

Considering the potential pro-regenerative capacity of 11,12-EET, we next set out to demonstrate the pro-regenerative capacity of 11,12-EET in vivo. The biosynthesis of 11,12-EET is catalysed by several synergistic enzymes from the cytochrome P450 pathway, making it difficult to increase 11,12-EET biosynthesis by manipulation of a specific gene³¹. However, soluble epoxide hydrolase (encoded by *Ephx2*) hydrolyses epoxyeicosatrienoic acids to non-bioactive dihydroxyeicosatrienoic

acids (Extended Data Fig. 5k), and its ablation causes the accumulation of epoxyeicosatrienoic acid³². We therefore generated *Ephx2^{CKO}* (*Ephx2^{fl/fl}*-Lyz2-cre) mice to evaluate the effect of 11,12-EET accumulation in vivo (Extended Data Fig. 6a). *Ephx2^{CKO}* mice showed accelerated muscle regeneration, with reduced muscle necrosis and regenerating area (Fig. 4a,b), enlarged distribution of myofibres (Fig. 4c,d and Extended Data Fig. 6b) and increased muscle strength and weight (Extended Data Fig. 6c,d). Consistently, *Ephx2* deficiency promoted the consecutive gene programs of the myogenic process of MuSCs (Fig. 4e and Extended Data Fig. 6e), with fewer MYH3⁺ early-regenerating myofibres at 6 dpi (Fig. 4f), indicating an enhanced regeneration process. Immunofluorescence staining further confirmed that myeloid knockout of *Ephx2* accelerated the proliferative capacity of MuSCs and MYOD and MYOG protein levels (Fig. 4g,h).

To assess whether this contribution of 11,12-EET accumulation to muscle regeneration is dependent on GSDMD, we crossed *Ephx2^{fl/fl}*-Lyz2-cre mice with *Gsdmd^{fl/fl}* mice, generating four genotypes including *Gsdmd^{CKO}Ephx2^{CKO}*, *Gsdmd^{het}Ephx2^{CKO}*, *Gsdmd^{CKO}Ephx2^{Het}* and *Gsdmd^{Het}Ephx2^{Het}* (used as littermate controls), and monitored their response to CTX-induced TA muscle injury (Fig. 4i). Further

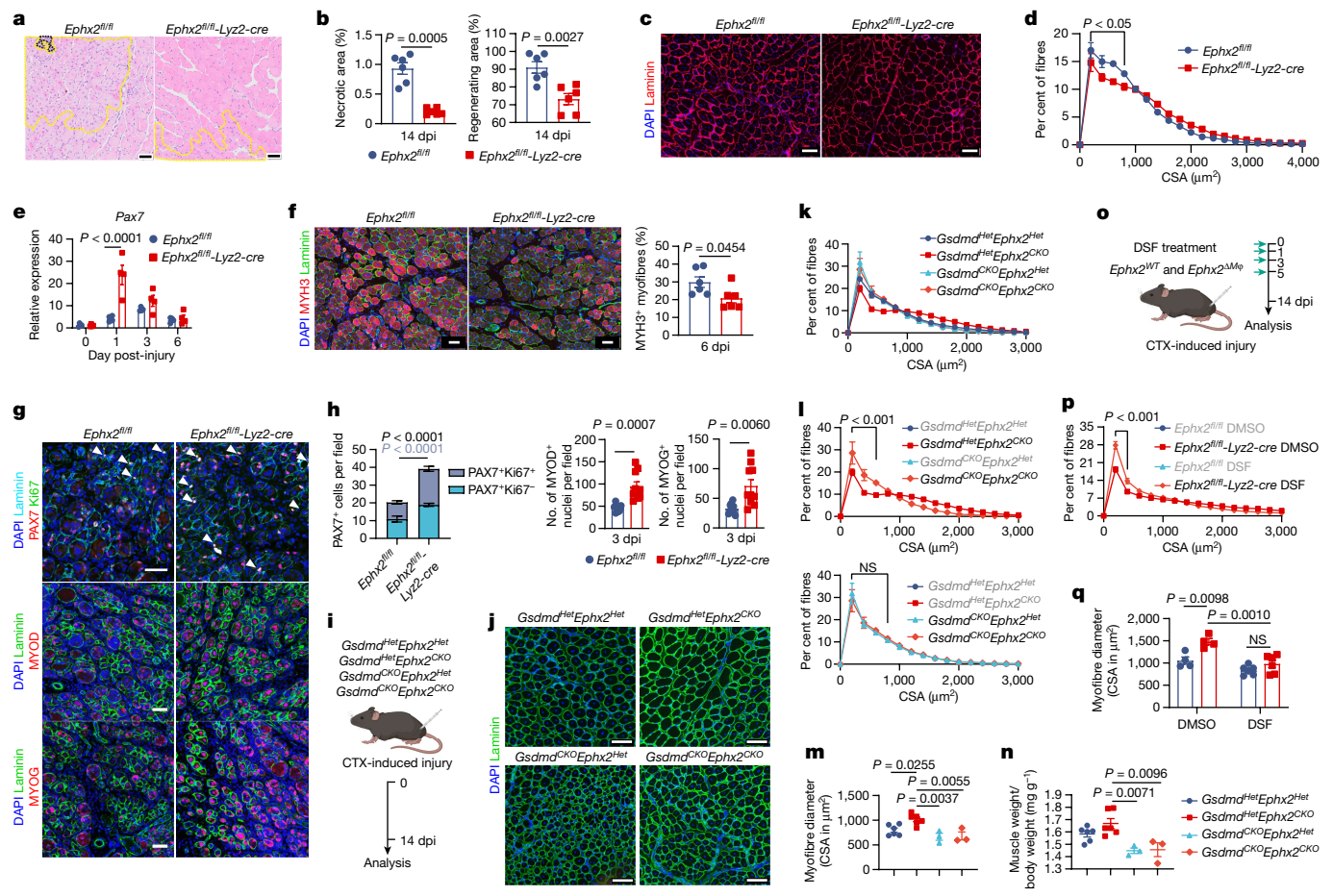


Fig. 4 | Accumulation of 11,12-EET promotes tissue regeneration in vivo. **a,b**, Representative H&E staining of TA muscle cross-sections at 14 dpi (**a**) and quantification of necrotic area (black dashed line in **a**) and regenerating area (yellow dashed line in **a**) ($n = 6$). **c,d**, Representative TA muscle CSA at 14 dpi (**c**) and frequency distribution (**d**) ($n = 5$). **e**, Expression of *Pax7* mRNA in muscle at the indicated dpi ($n = 4$). **f**, Representative immunofluorescence of *MYH3*⁺ myofibres at 6 dpi and quantification ($n = 6$). **g,h**, Representative immunofluorescence (**g**) and quantification (**h**) of quiescent ($n = 6$, *PAX7*^{Ki67}⁺) and proliferating ($n = 6$, *PAX7*^{Ki67}⁺) MuSCs, showing early ($n = 10$, *MYOD*⁺ nuclei) and late ($n = 10$, *MYOG*⁺ nuclei) differentiation markers at 3 dpi. White arrowheads indicate *PAX7*^{Ki67}⁺ MuSCs. Scale bars, 50 μ m. **i,j**, Schematic of

CTX-induced injury experiments in *Gsdmd*^{CKO}/*Ephx2*^{CKO} and littermate control mice (**i**), with representative immunostaining of TA muscle cross-sections at 14 dpi (**j**). **k–m**, The distribution frequency (**k,l**) and mean (**m**) of myofibre CSA. **n**, Mass of dissected TA muscles ($n = 3$, *Gsdmd*^{CKO}/*Ephx2*^{CKO} and *Gsdmd*^{CKO}/*Ephx2*^{Het}; $n = 6$, *Gsdmd*^{Het}/*Ephx2*^{CKO} and *Gsdmd*^{Het}/*Ephx2*^{Het}). **o–q**, Schematic of CTX injury model in *Ephx2*^{Het} and *Ephx2*^{CKO} mice with DSF or vehicle treatment (**o**) and distribution frequency (**p**) and mean of CSA (**q**) ($n = 4$, DMSO; $n = 6$, DSF) at 14 dpi. A representative (**a–g,j–n,p,q**) or a pool (**h**) of at least two independent experiments is shown. Unpaired two-tailed *t*-test (**b,f,h**); one-way ANOVA with Tukey's correction (**m,n**); two-way ANOVA with Šidák correction (**d,e,k,l,p,q**). Data are mean \pm s.e.m.

depletion of GSDMD hindered the beneficial effects of 11,12-EET accumulation found in *Ephx2*^{CKO} mice, resulting in a reduced myofibre size (Fig. 4j–m and Extended Data Fig. 6f,g) and muscle weight (Fig. 4n) at 14 dpi. In addition, no significant difference was observed between *Gsdmd*^{CKO}/*Ephx2*^{CKO} and *Gsdmd*^{CKO}/*Ephx2*^{Het} mice in general, morphologically. Accordingly, administration of disulfiram (DSF), an effective inhibitor of GSDMD pore formation³³, also counteracted the pro-regeneration effect on *Ephx2* deficiency (Fig. 4o–q and Extended Data Fig. 6h,i). These results demonstrated that the pro-regenerative potential of 11,12-EET released from macrophages requires the pore-forming function of GSDMD in vivo.

11,12-EET enhances FGF–FGFR signalling

To explore the mechanism of how 11,12-EET promotes muscle regeneration by upregulating the myogenic capacity of MuSCs, we isolated primary MuSCs to induce in vitro activation and sequential proliferation. The activation and proliferation of MuSCs are tightly regulated temporally^{17,23,34}. By profiling the transcriptome data, we found that 11,12-EET significantly boosted the activation and proliferation of

MuSCs, with increased expression of genes associated with cytoplasmic translation and mitochondrial respiratory activity, as well as several cell cycle-related (*H3c7* and *H2ac10*) and differentiated myosin (*Myh4* and *Mylpf*) genes (Fig. 5a,b). In addition, the gene expression pattern upon 11,12-EET treatment was positively correlated with activated MuSCs compared with their quiescent state (Extended Data Fig. 7a). Of note, at the timepoint at which 11,12-EET-treated MuSCs had entered the proliferative state, control MuSCs were still enriched with MAPK cascade and PI3K signalling (Fig. 5b), indicating that 11,12-EET accelerated activation of these signalling pathways during MuSC activation. In line with previous results, early-activated MuSCs had higher levels of FGF gene expression (*Fgfr1* and *Fgfr4*) compared with genes encoding other growth factor receptors (Extended Data Fig. 7b), indicating that the FGF–FGFR axis is one of the main signals within muscles that could activate the PI3K–AKT–mTOR and MAPK pathways³⁵. On the basis of this in silico analysis, we isolated MuSCs directly from CTX-injured TA muscles with or without 11,12-EET treatment at 3 dpi, and found that 11,12-EET treatment indeed induced increased activation levels of mTOR (phosphorylated (p)-AKT, p-p70S6K and p-4EBP) and MAPK (p-p38) signalling (Fig. 5c). Thus, we next set out to determine whether 11,12-EET affects

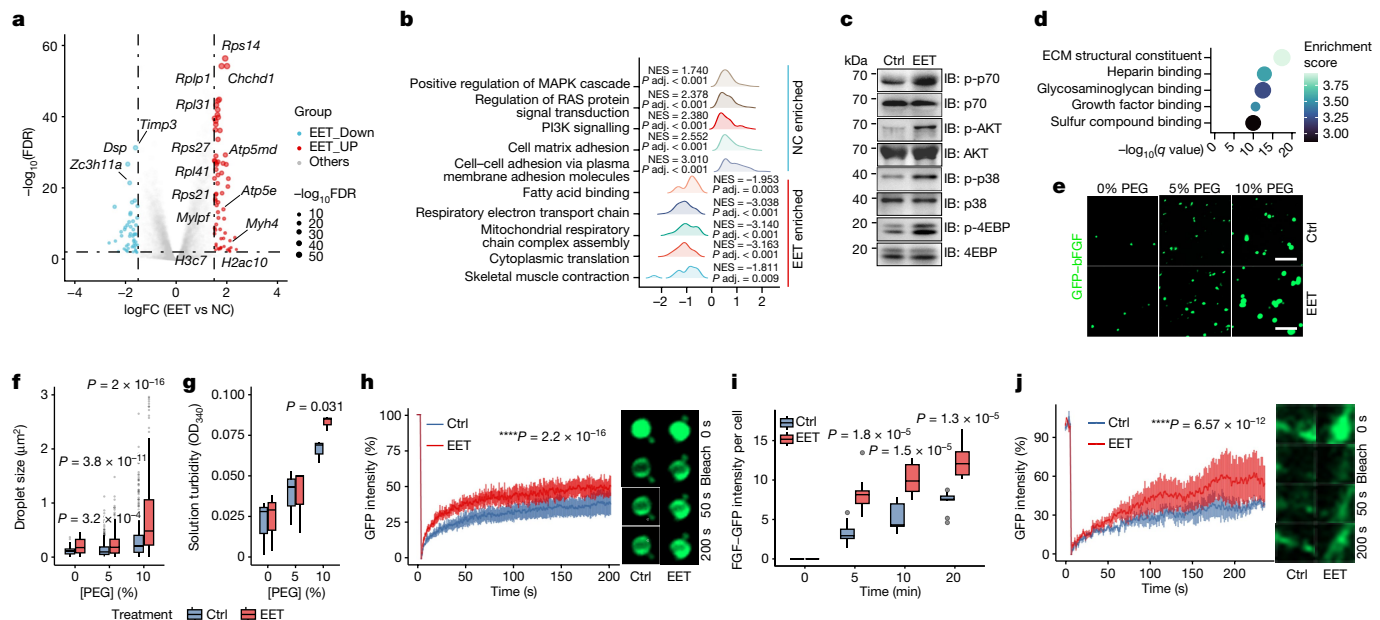


Fig. 5 | 11,12-EET promotes MuSC proliferation by enhancing FGF-FGFR signalling. **a,b**, Bulk RNA-seq analysis of MuSCs treated with 11,12-EET or vehicle (NC) for 2 days. Volcano plot of differentially expressed genes upon 11,12-EET treatment (**a**) and gene set enrichment analysis (GSEA) of MuSCs treated with 11,12-EET or vehicle (**b**). FDR, false discovery rate; NES, normalized enrichment score; Padj., adjusted *P* value. **c**, Western blot analysis of PI3K-AKT-mTOR and MAPK signalling downstream of FGF-FGFR in MuSCs freshly isolated from TA muscles post CTX injury and NIH-3T3 cells treated with FGF with or without 11,12-EET. Ctrl, control. **d**, Gene ontology (GO) term enrichment analysis of molecular function using the top 300 genes correlated with MuSC FGF signalling. **e–h**, Representative images (**e**) and size (**f**) of eGFP-bFGF phase separation with increasing concentrations of PEG with vehicle or 11,12-EET, and solution turbidity measured at 340 nm (**g**). Scale bars, 5 μm. Representative FRAP curve of eGFP-bFGF droplets (**h**). **i,j**, Intensity (**i**) and FRAP curve (**j**) of FGF condensates on the cell surface. **c,e,g–j**, A representative of at least two independent experiments is shown. Unpaired two-tailed *t*-test (**f,g,i**); one-way ANOVA (**h,j**). Data are mean ± s.e.m.

the upstream FGF-FGFR axis. Of note, 11,12-EET directly amplified FGF signalling with increased activation of the MAPK and PI3K-AKT-mTOR pathways in FGF-responsive NIH-3T3 cells (Extended Data Fig. 7c), and this amplification could be effectively inhibited by a FGFR inhibitor (Extended Data Fig. 7d). By contrast, 11,12-EET had minimal effect on the EGF-EGFR axis (Extended Data Fig. 7e).

During muscle regeneration, specific strategies are required to amplify signalling transduction to achieve sufficient pro-regeneration processes, owing to the limited intramuscular concentration of multiple ligands^{36,37}. We thus ranked the correlation level between each gene with the FGF signalling score using MuSC single-cell RNA-seq (scRNA-seq) data to identify potential cellular programs required for FGF signal amplification (Extended Data Fig. 7f). We found that the top genes that were positively correlated with higher FGF signalling were significantly enriched with gene terms such as extracellular structure and growth factor binding capacity (Fig. 5d and Extended Data Fig. 7g), which are required for the sufficient initiation and transduction of FGF-FGFR signalling³⁸ and closely related to the biochemical characteristics of FGF³⁹. Specifically, the disordered N- and C-terminal sequences of FGF facilitate its oligomerization, which provides sufficient multivalent weak interactions for liquid–liquid phase separation on the cell membrane surface^{40,41}. We therefore hypothesized that 11,12-EET, as a lipid, may enhance FGF phase separation on the membrane surface to efficiently amplify downstream signalling. We first used polyethylene glycol (PEG-8000) as a crowding agent, and found that 11,12-EET supplementation significantly increased PEG-induced eGFP–basic FGF (bFGF) droplet formation (Fig. 5e,f) and solution turbidity (Fig. 5g). Fluorescence recovery after photobleaching (FRAP) data further showed that 11,12-EET enhanced the fluorescence recovery of FGF droplets, indicating higher fluidity (Fig. 5h). On the basis of results from the cell-free system, we next set out to determine whether this effect occurs on the cell surface. Notably, we found that 11,12-EET enhanced

analysis of molecular function using the top 300 genes correlated with MuSC FGF signalling. **e–h**, Representative images (**e**) and size (**f**) of eGFP-bFGF phase separation with increasing concentrations of PEG with vehicle or 11,12-EET, and solution turbidity measured at 340 nm (**g**). Scale bars, 5 μm. Representative FRAP curve of eGFP-bFGF droplets (**h**). **i,j**, Intensity (**i**) and FRAP curve (**j**) of FGF condensates on the cell surface. **c,e,g–j**, A representative of at least two independent experiments is shown. Unpaired two-tailed *t*-test (**f,g,i**); one-way ANOVA (**h,j**). Data are mean ± s.e.m.

the bright condensates that formed on the edges of cells after incubation with eGFP-bFGF (Fig. 5i and Extended Data Fig. 7h), and increase the liquid-like characteristics of these condensates (Fig. 5j). Biochemical experiments further demonstrated that 11,12-EET enhanced FGF oligomerization, thereby promoting its signal transduction capacity (Extended Data Fig. 7i). Together, these data showed that 11,12-EET amplified FGF-FGFR signalling by enhancing FGF phase separation on the membrane surface.

As the activation capacity and proliferation level of MuSCs within the *in vitro* culturing system cannot fully represent the dynamics of *in vivo* MuSCs during injury, we injected saline or 11,12-EET intramuscularly to CTX-injured mice, with or without interperitoneal injection of an FGFR inhibitor (Extended Data Fig. 7j). Our results demonstrated that 11,12-EET effectively enhanced the activation of the FGF-FGFR signalling pathway *in vivo*, which was significantly inhibited by FGFR inhibition (Extended Data Fig. 7k). In addition, physiological accumulation of 11,12-EET induced by EPHX2 deficiency in myeloid cells promoted FGF-FGFR signalling cascades (Extended Data Fig. 7l).

Next, we conducted single-cell sequencing analyses on muscles treated with 11,12-EET (Extended Data Figs. 7j and 8a–c). We identified six MuSC-derived cell types (Extended Data Fig. 8d,e), and 11,12-EET injection led to increased numbers of differentiated *Myod1*^{high} and *MyoG*^{high} MuSCs post-injury (Extended Data Fig. 8d), accelerating both proliferation as well as differentiation of MuSC lineages (Extended Data Fig. 8f,g). Enrichment analysis further showed that 11,12-EET upregulated FGF binding capacity and downstream signalling in MuSCs (Extended Data Fig. 8h). Moreover, we found that 11,12-EET treatment increased the correlation between FGF binding and the p38 MAPK cascade, whereas *Gsdmd* deficiency reduced this correlation (Extended Data Fig. 8i), indicating that 11,12-EET amplified FGF-FGFR signalling cascades by promoting FGF binding capacity *in vivo*. Thus, using biochemical experiments and *in silico* data, we demonstrated that

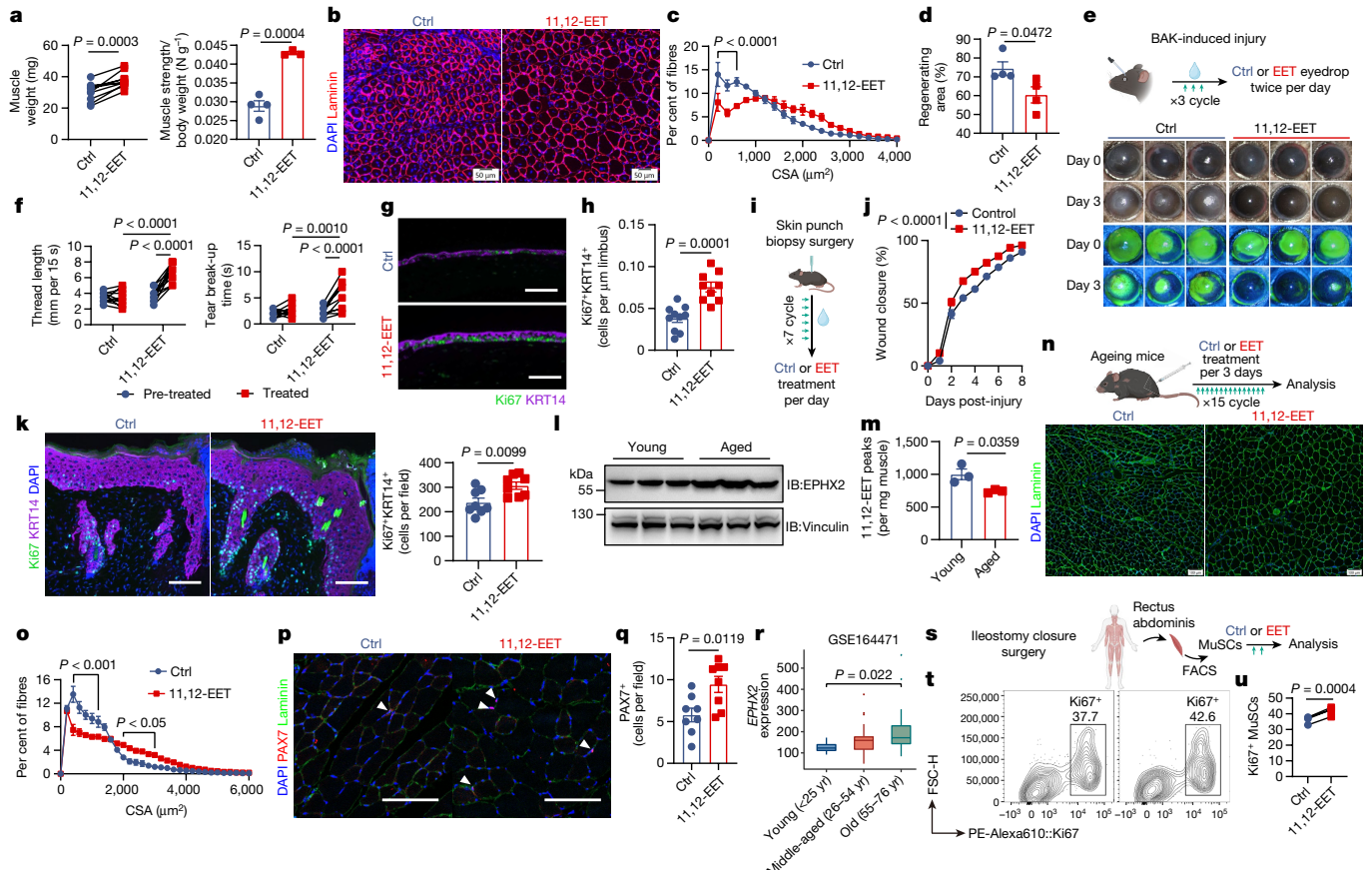


Fig. 6 | 11,12-EET exhibits pro-regeneration capacity in multiple organs. **a–d**, Muscle weight ($n = 10$), strength ($n = 4$ control, $n = 3$ 11,12-EET) (**a**), myofibre immunofluorescence (**b**) and CSA (**c**) ($n = 4$), and regenerating area ($n = 4$) (**d**) of TA muscles at 14 dpi with or without 11,12-EET. **e–h**, Schematic of the BAK-induced cornea injury model treated with or without 11,12-EET eyedrop (50 ng) twice for 3 days (**e**, top) and representative images of cornea and corneal fluorescein staining before and after treatment (**e**, bottom). **f**, Thread length and tear break-up time at day 3. **g,h**, Representative images of Ki67⁺ corneal limbus progenitor cells with or without 11,12-EET treatment (**g**) and quantification of Ki67⁺KRT14⁺ cells (**h**) ($n = 10$). **i–k**, Schematic of the skin punch biopsy model (**i**); mice were treated with or without 11,12-EET topically (300 ng) for 7 days. **j**, Wound closure over time ($n = 16$, control; $n = 18$, 11,12-EET). **k**, Immunofluorescence (left) and number of mouse Ki67⁺ epidermal progenitors ($n = 8$) post-injury with or without 11,12-EET. **l,m**, Immunoblot

showing EPHX2 expression (**l**) and 11,12-EET content (**m**) in muscle from young and aged mice ($n = 3$). **n–q**, Schematic of intramuscular supplementation with or without indicated treatment ageing mice and representative muscle cross-sections (**n**) and frequency distribution of fibre CSA (**o**) ($n = 8$). **p,q**, Representative images (**p**) and quantification (**q**) of MuSCs ($n = 8$). White arrowheads indicate PAX7⁺ MuSCs. **r–u**, Human muscle experiments. **r**, EPHX2 expression in human muscle samples. **s**, Schematic of human MuSC collection and isolation. **t,u**, Representative contour plots (**t**) and quantification (**u**) of Ki67⁺ levels in isolated human MuSCs following the indicated treatment ($n = 4$). A representative (**a**, left, **b–h,k,p,t**) or a pool (**a**, right, **j,q,u**) of at least two independent experiments is shown. Unpaired two-tailed *t*-test (**a**, right, **d,h,k,m,q,r**); paired two-tailed *t*-test applied (**a**, left, **u**); two-way ANOVA with Sidák correction (**c,f,j,o**). Data are mean \pm s.e.m. Scale bars: 50 μm (**b**), 100 μm (**e,g,k,n,p**).

11,12-EET amplifies FGF–FGFR signalling by enhancing liquid–liquid phase separation of FGF.

EET promotes regeneration in various models

Finally, we set out to examine the therapeutic potential of 11,12-EET for tissue repair *in vivo*. Intramuscular injection of 11,12-EET significantly improved muscle regeneration, with increased muscle weight and strength (Fig. 6a) and larger myotube diameter (Fig. 6b,c and Extended Data Fig. 9a), and reduced necrotic and early-regenerating areas at 14 dpi (Fig. 6d and Extended Data Fig. 9b). Additionally, we noted enhanced inflammation resolution (Extended Data Fig. 9c) and fewer MYH3⁺ myofibres (Extended Data Fig. 9d) at the late stage of regeneration in 11,12-EET-treated muscle. Of note, we further confirmed that the pro-regenerative capacity of 11,12-EET is FGFR dependent (Extended Data Fig. 9e–g).

Given the broad pro-regeneration capacity of FGF in various tissue regeneration processes such as corneal and skin injury^{38,42}, we next

tested whether 11,12-EET promotes tissue regeneration in other injury models. We established a corneal injury model by administering an overdose of the ophthalmic formulation benzalkonium chloride (BAK), which leads to dry eye symptoms and corneal epithelium damage⁴³. Eyedrop-based 11,12-EET treatment significantly reduced damage to the epithelium, as indicated by corneal sodium fluorescein staining (Fig. 6e), and improved clinical manifestations such as the amount of tear secretion and tear film stability (Fig. 6f). Pathological analysis further showed that 11,12-EET treatment ameliorated corneal thickening (Extended Data Fig. 9h,i) and reduced inflammatory cell infiltration at the late stage (Extended Data Fig. 9j–l), which hinders successful cornea regeneration, resulting in corneal fibrosis and other complications. Of note, 11,12-EET treatment significantly increased the proliferation of KRT14⁺ corneal limbus progenitor cells⁴⁴, indicating enhanced corneal epithelium regeneration (Fig. 6g,h). Furthermore, topical administration of 11,12-EET also significantly enhanced the wound closure rate in a skin punch biopsy-induced skin injury model (Fig. 6i,j, Extended Data Fig. 9m), which was coupled with increased

Article

Ki67 signals in local basal epidermal progenitor cells (Fig. 6k). Similarly, in a UV-induced skin injury model (Extended Data Fig. 10a), 11,12-EET treatment led to a significant attenuation in pinna swelling (Extended Data Fig. 10b,c) and decreased leukocytic infiltration (Extended Data Fig. 10d).

Although the age-related decline in tissue regenerative capacity is multifactorial⁴⁵, we explored whether 11,12-EET has physiological relevance to defects in age-related repair. Notably, we observed increased expression of EPHX2 in aged muscle (Fig. 6l and Extended Data Fig. 10e), resulting in a decreased level of intramuscular 11,12-EET (Fig. 6m). Next, we supplemented aged mice with 11,12-EET or vehicle intramuscularly every 3 days for 15 cycles (Fig. 6n). 11,12-EET supplementation resulted in a moderate reduction of age-induced fibrosis (Extended Data Fig. 10f), rejuvenated aged muscles with increased weight and strength (Extended Data Fig. 10g), and increased myofibre CSA (Fig. 6n,o and Extended Data Fig. 10h,i). These beneficial effects may be attributable to expansion of the satellite cell pool owing to local elevation of the 11,12-EET concentration (Fig. 6p,q). On the basis of these data from mouse models, we analysed EPHX2 expression in aged human muscles using a public dataset, and found that EPHX2 expression increased with age (Fig. 6r), suggesting that the accumulation of 11,12-EET may also be physiologically relevant to human muscle ageing. Finally, we set out to determine whether 11,12-EET could boost proliferation of human MuSCs. We isolated human MuSCs from muscle debris resulting from human ileostomy closure surgery⁴⁶ (Fig. 6s). Consistent with the data from mouse MuSCs, we found that 11,12-EET treatment significantly increased the proliferation capacity of human MuSCs from all four samples (Fig. 6t,u), supporting the therapeutic potential of 11,12-EET for promoting muscle regeneration in humans. In sum, we have shown, using multiple injury models in mouse as well as human data, that 11,12-EET—a metabolite released via GSDMD pores—exhibits pro-repair activity and has the capacity to rejuvenate aged muscle.

Discussion

Previous studies have indicated that hyperactivated macrophages may actively secrete small molecules via GSDMD pores that exert specific actions on neighbouring cells, resulting in increased muscle cell vitality. In this study, we used an unbiased screening strategy to systematically profile the secretome of hyperactivated cells, revealing that macrophages actively secrete metabolites during regeneration to establish immune–MuSC crosstalk in a GSDMD-dependent manner (Extended Data Fig. 10j). This work expands the range of metabolites that are known to act as signalling molecules⁴⁷.

Successful tissue regeneration requires a coordinated temporal sequence of initial inflammation, clearance of debris and amplification of local cells to set up the wound-healing milieu, followed by resolution and reestablishment of haemostasis^{1,2}. Here we identified 11,12-EET as a representative bioactive lipid that is secreted from hyperactivated macrophages during the early stage post-injury and serves as a tissue messenger to boost MuSC myogenesis. Moreover, our identification of distinct patterns of intramuscular metabolites in the secretome during regeneration suggests that metabolic interplay has a key role as a regulator of tissue regeneration. Systematic analysis of these metabolites and their functions in regeneration could be instructive in depicting the cell–cell crosstalk that facilitates wound healing. Ageing is usually accompanied by a marked loss of regeneration capacity, and we found that the aged muscle accumulates EPHX2, leading to decreased 11,12-EET. Our data indicate that dysregulation of the intramuscular metabolite landscape is a causative factor for ageing-related defects in repair, highlighting the pleiotropic beneficial effects of metabolite-mediated immune cell–MuSC crosstalk in modulating muscle rejuvenation and providing therapeutic insights for improving the clinical outcomes of stem cell-based therapy.

Online content

Any methods, additional references, Nature Portfolio reporting summaries, source data, extended data, supplementary information, acknowledgements, peer review information; details of author contributions and competing interests; and statements of data and code availability are available at <https://doi.org/10.1038/s41586-024-08022-7>.

1. Gurtner, G. C., Werner, S., Barrandon, Y. & Longaker, M. T. Wound repair and regeneration. *Nature* **453**, 314–321 (2008).
2. Eming, S. A., Murray, P. J. & Pearce, E. J. Metabolic orchestration of the wound healing response. *Cell Metab.* **33**, 1726–1743 (2021).
3. Xia, S. et al. Gasdermin D pore structure reveals preferential release of mature interleukin-1. *Nature* **593**, 607–611 (2021).
4. Devant, P. & Kagan, J. C. Molecular mechanisms of gasdermin D pore-forming activity. *Nat. Immunol.* **24**, 1064–1075 (2023).
5. Evavold, C. L. et al. The pore-forming protein gasdermin D regulates interleukin-1 secretion from living macrophages. *Immunity* **48**, 35–44.e36 (2018).
6. Martin, P. Wound healing—aiming for perfect skin regeneration. *Science* **276**, 75–81 (1997).
7. Shang, M. et al. Macrophage-derived glutamine boosts satellite cells and muscle regeneration. *Nature* **587**, 626–631 (2020).
8. Medzhitov, R. The spectrum of inflammatory responses. *Science* **374**, 1070–1075 (2021).
9. Broz, P., Pelegrin, P. & Shao, F. The gasdermins, a protein family executing cell death and inflammation. *Nat. Rev. Immunol.* **20**, 143–157 (2020).
10. Liu, X. & Lieberman, J. Knocking 'em dead: pore-forming proteins in immune defense. *Annu. Rev. Immunol.* **38**, 455–485 (2020).
11. Weindel, C. G., Ellzey, L. M., Martinez, E. L., Watson, R. O. & Patrick, K. L. Gasdermins gone wild: new roles for GSDMs in regulating cellular homeostasis. *Trends Cell Biol.* **33**, 773–787 (2023).
12. Li, M. et al. Gasdermin D maintains bone mass by rewiring the endo-lysosomal pathway of osteoclastic bone resorption. *Dev. Cell* **57**, 2365–2380.e2368 (2022).
13. Zhang, J. et al. Epithelial gasdermin D shapes the host-microbial interface by driving mucus layer formation. *Sci. Immunol.* **7**, eabk2092 (2022).
14. Karmakar, M. et al. N-GSDMD trafficking to neutrophil organelles facilitates IL-1 β release independently of plasma membrane pores and pyroptosis. *Nat. Commun.* **11**, 2212 (2020).
15. Chen, Y. et al. Gasdermin D drives the nonexosomal secretion of galectin-3, an insulin signal antagonist. *J. Immunol.* **203**, 2712–2723 (2019).
16. Tidball, J. G. Regulation of muscle growth and regeneration by the immune system. *Nat. Rev. Immunol.* **17**, 165–178 (2017).
17. Sousa-Victor, P., Garcia-Prat, L. & Munoz-Canoves, P. Control of satellite cell function in muscle regeneration and its disruption in ageing. *Nat. Rev. Mol. Cell Biol.* **23**, 204–226 (2022).
18. Relai, F. et al. Perspectives on skeletal muscle stem cells. *Nat. Commun.* **12**, 692 (2021).
19. Tierney, M. T. & Sacco, A. Satellite cell heterogeneity in skeletal muscle homeostasis. *Trends Cell Biol.* **26**, 434–444 (2016).
20. Zhang, J. et al. Endothelial lactate controls muscle regeneration from ischemia by inducing M2-like macrophage polarization. *Cell Metab.* **31**, 1136–1153.e1137 (2020).
21. Nakka, K. et al. JMJD3 activated hyaluronan synthesis drives muscle regeneration in an inflammatory environment. *Science* **377**, 666–669 (2022).
22. Qiu, X. et al. Reversed graph embedding resolves complex single-cell trajectories. *Nat. Methods* **14**, 979–982 (2017).
23. Massenet, J., Gardner, E., Chazaud, B. & Dilworth, F. J. Epigenetic regulation of satellite cell fate during skeletal muscle regeneration. *Skelet. Muscle* **11**, 4 (2021).
24. De Micheli, A. J. et al. Single-cell analysis of the muscle stem cell hierarchy identifies heterotypic communication signals involved in skeletal muscle regeneration. *Cell Rep.* **30**, 3583–3595.e3595 (2020).
25. Kayagaki, N. et al. NINJ1 mediates plasma membrane rupture during lytic cell death. *Nature* **591**, 131–136 (2021).
26. Degen, M. et al. Structural basis of NINJ1-mediated plasma membrane rupture in cell death. *Nature* **618**, 1065–1071 (2023).
27. Cui, M., Cheng, C. & Zhang, L. High-throughput proteomics: a methodological mini-review. *Lab. Invest.* **102**, 1170–1181 (2022).
28. Zanoni, I., Tan, Y., Di Gioia, M., Springstead, J. R. & Kagan, J. C. By capturing inflammatory lipids released from dying cells, the receptor CD14 induces inflammasome-dependent phagocyte hyperactivation. *Immunity* **47**, 697–709.e693 (2017).
29. Borges, J. P. et al. Glycine inhibits NINJ1 membrane clustering to suppress plasma membrane rupture in cell death. *eLife* **11**, e78609 (2022).
30. Liu, X. et al. Context-dependent activation of STING-interferon signaling by CD11b agonists enhances anti-tumor immunity. *Cancer Cell* **41**, 1073–1090.e1012 (2023).
31. Dennis, E. A. & Norris, P. C. Eicosanoid storm in infection and inflammation. *Nat. Rev. Immunol.* **15**, 511–523 (2015).
32. Edin, M. L. et al. Epoxide hydrolase 1 (EPHX1) hydrolyzes epoxyeicosanoids and impairs cardiac recovery after ischemia. *J. Biol. Chem.* **293**, 3281–3292 (2018).
33. Hu, J. J. et al. FDA-approved disulfiram inhibits pyroptosis by blocking gasdermin D pore formation. *Nat. Immunol.* **21**, 736–745 (2020).
34. Palacios, D. et al. TNF/p38 α /Polycomb signaling to Pax7 locus in satellite cells links inflammation to the epigenetic control of muscle regeneration. *Cell Stem Cell* **7**, 455–469 (2010).
35. Xie, Y. et al. FGF/FGFR signaling in health and disease. *Signal Transduct. Target. Ther.* **5**, 181 (2020).

36. Do, M. K. et al. Time-coordinated prevalence of extracellular HGF, FGF2 and TGF- β 3 in crush-injured skeletal muscle. *Anim. Sci. J.* **83**, 712–717 (2012).
37. Rodgers, J. T. et al. mTORC1 controls the adaptive transition of quiescent stem cells from G₀ to G_{Alert}. *Nature* **510**, 393–396 (2014).
38. Maddaluno, L., Urwyler, C. & Werner, S. Fibroblast growth factors: key players in regeneration and tissue repair. *Development* **144**, 4047–4060 (2017).
39. Richardson, T. P., Trinkaus-Randall, V. & Nugent, M. A. Regulation of basic fibroblast growth factor binding and activity by cell density and heparan sulfate. *J. Biol. Chem.* **274**, 13534–13540 (1999).
40. Xue, S. et al. Phase separation on cell surface facilitates bFGF signal transduction with heparan sulphate. *Nat. Commun.* **13**, 1112 (2022).
41. Venkataraman, G. et al. Preferential self-association of basic fibroblast growth factor is stabilized by heparin during receptor dimerization and activation. *Proc. Natl Acad. Sci. USA* **93**, 845–850 (1996).
42. Beenken, A. & Mohammadi, M. The FGF family: biology, pathophysiology and therapy. *Nat. Rev. Drug Discov.* **8**, 235–253 (2009).
43. Goldstein, M. H., Silva, F. Q., Blender, N., Tran, T. & Vantipalli, S. Ocular benzalkonium chloride exposure: problems and solutions. *Eye* **36**, 361–368 (2022).
44. Park, M. et al. Visualizing the contribution of keratin-14⁺ limbal epithelial precursors in corneal wound healing. *Stem Cell Rep.* **12**, 14–28 (2019).
45. Neves, J., Sousa-Victor, P. & Jasper, H. Rejuvenating strategies for stem cell-based therapies in aging. *Cell Stem Cell* **20**, 161–175 (2017).
46. Benjamin, D. I. et al. Fasting induces a highly resilient deep quiescent state in muscle stem cells via ketone body signaling. *Cell Metab.* **34**, 902–918.e906 (2022).
47. Baker, S. A. & Rutter, J. Metabolites as signalling molecules. *Nat. Rev. Mol. Cell Biol.* **24**, 355–374 (2023).

Publisher's note Springer Nature remains neutral with regard to jurisdictional claims in published maps and institutional affiliations.

Springer Nature or its licensor (e.g. a society or other partner) holds exclusive rights to this article under a publishing agreement with the author(s) or other rightsholder(s); author self-archiving of the accepted manuscript version of this article is solely governed by the terms of such publishing agreement and applicable law.

© The Author(s), under exclusive licence to Springer Nature Limited 2024

Article

Methods

Mice

C57BL/6 J mice, *Gsdmd*^{KO}, *Gsdmd*^{f/f} and *Ephx2*^{f/f} mice were purchased from Gempharmatech. *Lyz2*-*cre* mice were purchased from the Jackson Laboratory. *Gsdmd*^{f/f} and *Ephx2*^{f/f} mice were crossed with *Lyz2*-*cre* mice to obtain *Gsdmd*^{f/f}-*Lyz2*-*cre* and *Ephx2*^{f/f}-*Lyz2*-*cre* mice. *Gsdmd*^{KO} mice and their littermate controls were only used for in vitro macrophage experiments unless otherwise stated. *Ephx2*^{f/f}-*Lyz2*-*cre* mice were crossed with *Gsdmd*^{f/f} mice to generate *Gsdmd*^{f/f}*Ephx2*^{f/f}-*Lyz2*-*cre* (*Gsdmd*^{Het}*Ephx2*^{KO}), *Gsdmd*^{f/f}*Ephx2*^{f/f}-*Lyz2*-*cre* (*Gsdmd*^{KO}*Ephx2*^{Het}) and littermate control *Gsdmd*^{f/f}*Ephx2*^{f/f}-*Lyz2*-*cre* (*Gsdmd*^{Het}*Ephx2*^{Het}). The mice were bred in a specific pathogen-free facility in the Laboratory Animal Center of Zhejiang University in accordance with the National Institute of Health Guide for the Care and Use of Laboratory Animals and housed on a 12-h light:12-h dark cycle at 22–24 °C with 40–70% humidity and ad libitum access to food and water for the duration of the experiment. The animal experimental protocols were approved by the Review Committee of Zhejiang University School of Medicine (ZJU20230356) and were in compliance with institutional guidelines. Mice of both sexes were used throughout the study; sex-matched and age-matched (8–12 weeks) controls were used in individual experiments.

Human MuSC isolation and culture

Human muscle samples were collected from patients who had undergone diverting ileostomy closure surgery at the Second Affiliation Hospital of Zhejiang University after patient consent. During standard surgery procedure, the surgeon would remove a small portion of rectus abdominis muscle to provide adequate space for tissue reconstruction and achieve optimal stoma retraction. Isolation and culture of human MuSC are based on a previous report⁴⁶. In brief, this muscle debris was collected and minced on ice, and transferred into 10 ml wash medium (Ham's F-10 supplemented with 10% v/v horse serum and 1% penicillin-streptomycin) containing (3,825 U per g muscle) collagenase II (Gibco). Tissues were digested in a 37 °C shaker for 1 h. The digestion was stopped by adding 40 ml cold wash medium. Cells were centrifuged at 500g for 5 min at 4 °C and the supernatant was aspirated. The pellet was resuspended and digested in wash medium containing 100 U ml⁻¹ collagenase II and 1 U ml⁻¹ dispase II (Gibco) for 30 min at 37 °C, then the digestion was stopped as noted above. Cells were then stained and sorted with CD56, CD31, CD45, and CD29 flow cytometry antibodies (CD31⁻CD45⁻CD29⁺CD56⁺). Sorted human MuSCs were seeded on 0.1 mg ml⁻¹ ECM gel (Sigma, E1270) and cultured in growth medium (Ham's F-10 supplemented with 20% FBS, 1% penicillin-streptomycin and 2.5 ng ml⁻¹ bFGF (Gibco, PHG0024)) with or without 5 μM 11,12-EET for 2 days. Then the human MuSCs were stained with Ki67 (eBioscience) and analysed by flow cytometry. All procedures conducted in this study have received ethical approval from the Human Research Ethics Committee of Second Affiliation Hospital of Zhejiang University (2024-0159).

Cell culture

NIH/3T3 and C2C12 cell lines were from the American Type Culture Collection. Cells were cultured in Dulbecco's modified Eagle's medium (DMEM) supplemented with 10% heat-inactivated FBS and 1% penicillin-streptomycin, unless otherwise indicated.

Primary mouse MuSCs were isolated as previously described⁴⁸. In brief, the hind limb muscles were detached, minced on ice, and transferred into 10 ml wash medium (Ham's F-10 supplemented with 10% v/v horse serum and 1% penicillin-streptomycin) containing 800 U ml⁻¹ collagenase II (Gibco). Tissues were digested in a 37 °C shaker for 1 h. The digestion was stopped by adding 40 ml cold wash medium. Then the cells were centrifuged at 500g for 5 min at 4 °C and the supernatant was aspirated. The pellet was resuspended and digested in wash

medium containing 100 U ml⁻¹ collagenase II and 1 U ml⁻¹ dispase II (Gibco) for 30 min at 37 °C, then the digestion was stopped as noted above. The fraction of isolated cells was sorted using a satellite cell isolation kit (Miltenyi Biotec, 130-104-268) according to the manufacturer's instructions. The counterpart of non-satellite cells was collected where needed as control. Isolated satellite cells were seeded on 0.1 mg ml⁻¹ ECM gel (Sigma, E1270) and cultured in growth medium (Ham's F-10 supplemented with 20% FBS, 1% penicillin-streptomycin and 2.5 ng ml⁻¹ bFGF (Gibco, PHG0024)) or in differentiation medium (DMEM supplemented with 5% horse serum and 1% penicillin-streptomycin) for the indicated time.

Mouse peritoneal macrophages were collected 4 days after intraperitoneal thioglycolate (Merck) injection of control and *Gsdmd*^{KO} mice, and then cultured in DMEM supplemented with 10% heat-inactivated FBS and 1% penicillin-streptomycin. For in vitro hyperactivated state induction, macrophages were primed with 500 ng ml⁻¹ LPS (Sigma, L2630) for 4 h in Opti-MEM (Gibco). Thirty minutes before the second signal, 10 mM glycine (Sigma), was supplemented. GSDMD activation was induced by adding 10 μM nigericin (30 min), or transfection with 1 μg ml⁻¹ poly(dA:dT) using Lipofectamine 2000 (3 ml mg⁻¹ DNA) following the manufacturer's instructions (Invitrogen). Nigericin (tlrl-nig) and poly(dA:dT) (tlrl-patn) were from Invitrogen. Supernatants and cells were collected for further analysis.

In vitro C2C12 cocultures with macrophage-conditioned medium

LPS-primed macrophages were subjected to nigericin and poly(dA:dT) for 30 min with glycine pre-treatment for 30 min, and the supernatants were collected and ultracentrifuged into <3 kDa and >3 kDa portions. C2C12 cells were cultured in proliferation and differentiation medium mixed with each supernatant fraction described above, which were replaced every two days. After 3 days of differentiation, myotubes were fixed with 4% paraformaldehyde and stained for myosin heavy chain. The fusion index (defined as the percentage of nuclei within myotubes, nuclei ≥2) and myotube size (defined as the mean number of nuclei in myotubes) were calculated.

CTX muscle injury

To create the CTX-induced injury model, mice were anaesthetized with isoflurane, followed by intramuscular injection of 50 μl of 8 μM CTX (Latoxan, L8102) into the TA muscle. Muscles were obtained for assessment at the indicated time after injury. 11,12-EET (Cayman, 50511, 500 ng per TA muscle) was injected intramuscularly and DSF (Med-ChemExpress, HY-B0240) treatment (50 mg per kg) was administered via intraperitoneal injection at the indicated timepoints. The vehicle was used as control.

Grip test

TA muscle strength was assessed by a force gauge (Chatillon, DF3 series digital force gauges). In brief, mice were pulled backwards with a continuous horizontal movement while they grasped the grid of the device firmly with their hind limbs. The measurement was replicated five times to calculate the average per mouse.

Muscle interstitial fluid collection

Muscle TIF was collected by centrifugation as previously described⁴⁸. In brief, TA muscles were isolated and placed on a 40-μm strainer, which was fixed in a 50 ml Falcon tube. Then two-step centrifugation was performed, 50g for 5 min at 4 °C to clear the remaining surface liquid, and 600g for 10 min at 4 °C to collect the interstitial fluid for further processing and analysis.

Mouse corneal and skin injury model

To create the corneal injury model, mice were administered eye-drops containing 5 μl of 0.2% (w/v) BAK (TCI, B0414) twice per day.

After 5 consecutive days, the mice were randomly divided into 2 groups: one was given topical eyedrops of 5 µl 11,12-EET (10 µg ml⁻¹), and the other was given vehicle, twice per day. To assess the therapeutic efficacy of 11,12-EET, the Schirmer test, tear break-up time (TBUT), and sodium fluorescein staining were applied after 3 cycles of treatment. In the Schirmer test, tear volume was measured with phenol red-impregnated cotton threads (Tianjin Jingming Tech) for 15 s following the manufacturer's instructions. TBUT was recorded in seconds when the first black spot was observed under a slit lamp (YZ5T, 66 Vision-Tech) with cobalt blue light. For sodium fluorescein staining, 2 µl of 1% sodium fluorescein (w/v, Jing Ming Tech) was applied to the lateral conjunctival sac of each eye. The corneal fluorescein staining was examined under slit lamp cobalt blue light. After treatment, the corneas were collected for H&E staining and immunofluorescence.

For the UV-induced skin injury model⁴⁹, mice were anaesthetized with isoflurane, shaved, and a depilatory (Veet cream) was applied. The ears were then exposed to UV ($\lambda = 254$ nm; voltage, 8 W; source 30 cm from the target) for 25 min. Two-hundred nanograms of 11,12-EET was applied topically every 3 days, and ear thickness was assessed (under isoflurane anaesthesia) every 3 days with a caliper and compared to the initial value.

For the skin punch biopsy, the protocol was performed as described previously with modification⁵⁰. In brief, mice were anaesthetized with isoflurane, shaved, depilated (Veet cream) and sterilized by Betadine. A full thickness cutaneous injury extending through the panniculus carnosus on dorsal side of mice was created by a sterile skin punch (5 mm). And Tegaderm is applied to cover the area of the open wound, and removed from the mice 24 h post-surgery. Three hundred nanograms 11,12-EET was applied topically every day, and wound measurement was recorded by photograph with ruler to calibration and analysed by ImageJ (Fiji).

Histology and immunofluorescence

TA muscles were isolated, fixed in 4% paraformaldehyde, and embedded in paraffin. Ten-micrometre sections were cut for H&E staining following deparaffinization and rehydration. Alternatively, muscles were dehydrated in 30% w/v sucrose for 30 min at 4 °C. Then Tissue-Tek OCT Compound (Sakura) was used to embed the muscles in a mould. OCT-embedded samples were quickly frozen in liquid nitrogen and processed using a cryostat (Thermo) to obtain 10-µm cryosections for immunostaining. In brief, cryosections were fixed in 4% paraformaldehyde for 10 min and permeabilized in a buffer containing 5% donkey serum and 0.2% Triton X-100 in PBS for 20 min at room temperature followed by treatment with retrieval solution pH 6.0 (Solarbio Life Science) at 95 °C for 20 min. After cooling to room temperature, sections were subjected to subsequent blocking by 5% donkey serum for 1 h at room temperature and mouse Fab fragment anti-mouse IgG (Jackson, 1:100) for 30 min at room temperature. The following primary antibodies were used to incubate the sections overnight at 4 °C: anti-PAX7 (DSHB, 1:200), anti-MYOD (Santa Cruz, 1:200), anti-myogenin (DSHB, 1:200), anti-Ki67 (Biologend, 1:200), anti-embryonic myosin (DSHB, 1:50), anti-F4/80 (CST, 1:200), anti-CD31 (Abcam, 1:500), and anti-laminin (Sigma, 1:500). The secondary antibodies were diluted (1:500) in PBS with 5% goat serum and incubated at room temperature for 1 h. The following secondary antibodies were used (Abcam): anti-rabbit IgG H&L-Alexa Fluor 488, anti-rabbit IgG H&L-Alexa Fluor 555, anti-mouse IgG H&L-Alexa Fluor 555, and anti-rabbit IgG H&L-Alexa Fluor 647. The slides were mounted with mounting buffer containing DAPI. Images were scanned under a VS200 (Olympus), and data were analysed by ImageJ. For histology annotation, each slide was evaluated blindly. The regenerating areas were identified by the dominant presence of fibres with centrally located nuclei and/or some remaining mononuclear cell infiltrates²⁰.

Detection of bFGF phase separation

The eGFP-bFGF protein was purified as described previously⁴⁰. The purified protein then was diluted to 1 mg ml⁻¹ in assay buffer (8 mM Na₂HPO₄, 2 mM KH₂PO₄, 136 mM NaCl, and 2.6 mM KCl, pH 7.2). To analyse the cell-free phase separation in vitro, 5 µM eGFP-bFGF was mixed with different concentrations of PEG-8000 (0–10% w/v) with or without 11,12-EET. Turbidity was measured by absorption at 340 nm using a Nanodrop 2000c (Thermo Fisher Scientific). For condensate formation on the cell surface, cells were starved in serum-free medium for 8 h, and 3 µM eGFP-bFGF was added to the starved cells with or without 11,12-EET for the indicated time at 37 °C; they were then fixed in 4% paraformaldehyde and stained with DAPI for further immunofluorescence staining.

Fluorescence recovery after photobleaching

For in vitro FRAP detection, a circular region of interest (ROI) located at the center of the droplets was photobleached to ~40% of the original intensity by illuminating the ROI with the laser, and then the eGFP-bFGF signal was consecutively recorded for a total of 250 s. For FRAP detection on the cell surface, NIH-3T3 cells were seeded onto a glass bottom cell culture dish and treated with 3 µM eGFP-bFGF for the indicated time. After three washes in PBS, eGFP-positive cells were selected to measure the eGFP signal intensity before and after photobleaching. A circular ROI at the cell membrane was photobleached to ~20% of the original intensity, and then the eGFP-bFGF signal was consecutively recorded for a total of 250 s. Images were acquired using a Zeiss LSM800 microscope fitted with a 40× or 100× objective.

ELISA and LDH assay

Supernatants were collected and the concentrations of IL-1β, IL-6, TNF (all from Thermo Fisher) and 11,12-EET (Abcam) were determined according to the manufacturer's instructions. The LDH level was determined using an LDH releasing assay (Promega), according to the manufacturer's instructions.

Immunoblot analysis

Protein extraction was used for immunoblot analysis as described previously⁵¹. Tissues were minced and ground in RIPA buffer (50 mM Tris pH 7.4, 150 mM NaCl, 1% Triton X-100, 1% sodium deoxycholate, and 0.1% SDS with complete protease inhibitor cocktail), and lysed for 20 min on ice followed by 12,000 rpm centrifugation for 10 min at 4 °C to collect supernatant. An equal volume of 5× SDS loading buffer (156 mM Tris-HCl, 5% SDS, 25% glycerol, 12.5% β-mercaptoethanol, and 0.0125% bromophenol blue) was added. The samples were boiled and separated on 10% or 12% SDS-PAGE gels and transferred to nitrocellulose membranes (Pall, 66485), which were blocked in Tris-Cl Buffered Saline Solution with 0.05% Tween-20 (TBST) containing 10% skimmed milk for 1 h at room temperature. The following primary antibodies were incubated: anti-GSDMD (Abcam, 1:1,000), anti-EPHX2 (Proteintech, 1:2,000), anti-p38 (CST, 1:1,000), anti-phospho-p38 (CST, 1:1,000), anti-ERK1/2 (CST, 1:1,000), anti-phospho-ERK1/2 (CST, 1:1,000), anti-AKT (CST, 1:1,000), anti-phospho-AKT (CST, 1:1,000), anti-FGFR1 (CST, 1:1,000), anti-phospho-FGFR1 (Abclonal, 1:1,000), anti-NINJ1 (Santa Cruz, 1:1,000), anti-p70S6K (Abclonal, 1:1,000), anti-phospho-4E-BP1(Thr37/46) (Cell Signaling Technology, 1:1,000), anti-eIF4EBP1 (Abclonal, 1:1,000) and anti-vinculin (Abcam, 1:1,000) at 4 °C overnight. After incubation with the appropriate horseradish peroxidase-conjugated secondary antibodies (1:5,000, Diagbio) for 1 h at room temperature, the signal was visualized with ECL reagents (FDbio) and detected by a chemiluminescence imaging system (Clinxsci), and the quantification of grey intensity was analysed by ImageJ (Fiji).

For gel source data and grey intensity analysis, see Supplementary Information.

Crosslinking assay

Crosslinking experiments were performed as described²⁶. The crosslinker BS³ was added to the tissue lysates (3 mM; Thermo Fisher) and incubated for 5 min at room temperature. Next, 20 mM Tris pH 7.5 solution was added to stop the reaction and incubated for another 15 min at room temperature. The lysates were then used for immunoblot.

RT-qPCR

Tissues were minced and ground, and total RNA was extracted using total RNA extraction reagent (Vazyme). Reverse transcription to complementary DNA was performed by HiScript II QRT SuperMix (Vazyme), according to the manufacturer's instructions. Quantitative PCR was assessed by ChamQ Universal SYBR qPCR Master Mix on a LightCycler 480 II (Roche). All samples were normalized to GAPDH. The primers used were as follows: *Pax7*: forward, 5'-GCTACCAGTACAGCCAGTATG-3'; reverse, 5'-GTCACTAACATGGTAGATG-3'. *Myod1*: forward, 5'-GCT ACCAGTACAGCCAGTATG-3'; reverse, 5'-GTTCCCTGTTCTGTGCGCT-3'. *Myog*: forward, 5'-ATGGTGCCAGTGAATGCAA-3'; reverse, 5'-ACC CAGCCTGACAGACAATC-3'. *Gapdh*: forward, 5'-AGGTCGGTGTGA ACGGATTG-3'; reverse, 5'-TGTAGACCATGTAGTTGAGGTCA-3'.

Flow cytometry

Single-cell suspensions were obtained from TA muscles as described above. Cells were blocked with anti-mouse CD16/CD32 Fc Block (BD Biosciences) for 15 min on ice and incubated with the indicated primary antibodies, anti-CD45 (APC-Cy7), anti-F4/80 (APC), anti-CD11b (PE-Cy7), anti-Ly6C (BV785), and anti-Ly6G (FITC) according to the manufacturer's instructions. Live cells were determined using fixable viability dyes (FVS). Cells were analysed with a NovoCyte (ACEA) or BD Fortessa flow cytometer. Data were analysed using FlowJo 10 software.

Bulk RNA-seq library preparation and analysis

Primary MuSCs were isolated and cultured with or without 11,12-EET for 2 days. Total RNA was isolated and purified using TRIzol reagent (Invitrogen) following the manufacturer's procedure. The amount and purity of each RNA sample was quantified with NanoDrop ND-1000 (NanoDrop) and RNA integrity was assessed by Bioanalyzer 2100 (Agilent) with RNA integrity number >7.0, and further confirmed by electrophoresis with denaturing agarose gel. Poly (A) RNA was purified from 1 µg total RNA using Dynabeads Oligo (dT) (25–61005, Thermo Fisher) using two rounds of purification, followed by fragmentation using the Magnesium RNA Fragmentation Module (e6150, NEB) at 94 °C for 5–7 min. Cleaved RNA fragments were reverse-transcribed to create the cDNA with SuperScript II Reverse Transcriptase (1896649, Invitrogen), which were next used to synthesize U-labelled second-stranded DNAs with *Escherichia coli* DNA polymerase I (m0209, NEB), RNase H (m0297, NEB) and dUTP Solution (R0133, Thermo Fisher). After PCR amplification, the average insert size for the final cDNA library was 300 ± 50 bp. Finally, 2× 150 bp paired-end sequencing (PE150) on an Illumina Novaseq 6000 was performed following the vendor's recommended protocol. An RNA library was prepared with the assistance of LC-Bio Technology.

In downstream analysis, FastQC was used for quality control with default parameters. After adaptor trimming with Cutadapt, read pairs with length >30 bp were kept, and aligned to the mouse reference genome GRCm38.102 using star. Differentially expressed genes were called using DESeq2. GSEA was applied with ClusterProfiler according to the default pipeline⁵². Volcano plots and other visualizations were based on ggplot2.

Single-cell library preparation and sequencing

TA muscle tissue was collected from mice with the indicated treatment or genotype. After washing with ice-cold PBS, the tissue was minced

into 2–3 mm pieces and washed twice with ice-cold PBS. Digestion was performed with digestion buffer (0.5 mg ml⁻¹ Collagenase I (Sigma), 0.5 mg ml⁻¹ Collagenase V (Sigma), and 0.5 mg ml⁻¹ Dispase (Worthington)) at 37 °C with 100 rpm for 10 min, and stopped with an equal volume of ice-cold PBS containing 10% FBS. Cell suspensions were passed through a 70–30 µm filter twice, counted with a cell counter (Countstar), and centrifuged at 400g for 6 min at 12 °C. Cells were resuspended with RPMI1640 (Gibco) on ice. The remaining muscle tissue was digested with 6 ml 0.25% Trypsin-EDTA at 37 °C with 100 rpm for 10 min, and stopped with an equal volume of ice-cold PBS containing 10% FBS, followed by 2 PBS washes and passage through 70–30 µm filters. The two cell fractions were collected and red blood cells were removed using 4 ml red blood cell lysis solution. Then the suspension was resuspended in 1× PBS (0.04% BSA) and centrifuged twice at 300g for 3 min at 4 °C. The cell pellet was resuspended in 50 µl of 1× PBS (0.04% BSA). Overall cell viability was confirmed by trypan blue exclusion, which was required to be >85%, single-cell suspensions were counted using a cell counter, and the final concentration was adjusted to 700–1200 cells per µl.

The single-cell suspensions were loaded to 10x Chromium to capture 8,000–10,000 single cells according to the manufacturer's instructions with the 10X Genomics Chromium Single-Cell 3' kit (V3). The subsequent cDNA amplification and library construction steps were performed according to the standard protocol. Libraries were sequenced on an Illumina NovaSeq 6000 sequencing system (paired-end multiplexing run, 150 bp) by LC-Bio Technology at a minimum depth of 20,000 reads per cell.

Single-cell data analysis

Sequencing results were demultiplexed and converted to FASTQ format using Illumina bcl2fastq software (v2.20). Sample demultiplexing, barcode processing, and single-cell 3' gene counting was performed with Cell Ranger (version 3.1.0), and scRNA-seq data were aligned to the Ensembl genome GRCm38 reference genome. The pipelines were run with the assistance of LC-Bio Technology.

Downstream analysis was performed with the Seurat package (v4.0.1)⁵³. Low-quality cells with <200 or >1,000 genes detected and cells with mitochondrial encoded transcripts representing >20% were excluded from analysis. The raw gene expression matrix after quality control was cell-normalized over total expression, and 2,000 variable features were selected for the integration of 6 samples (WT_CON, WT_Day2, WT_Day10, KO_CON, KO_Day2, and KO_Day10) in *Gsdmd*^{fl/fl} versus *Gsdmd*^{CKO} analysis; while using 3,000 variable features for the integration of 5 samples (WT_CON, Mock_Day3, Mock_Day10, EET_Day3, and EET_Day10) in 11,12-EET treatment analysis. Anchors were identified using the FindIntegrationAnchors function followed by the Integrate-Data function with normalization.method = 'SCT' and dims = '30'. We regressed for the following confounding factors: cell cycle (determined by CellCycleScoring) and percentage of ribosome genes. FindAllMarkers was used to determine the signature marker genes of each cluster, and each cell type was determined based on known markers. For *Gsdmd*^{fl/fl} versus *Gsdmd*^{CKO} analysis, C01_Mac (*Lyz2*, *C1qb*), C02_Mono (*Plac8*, *Ly6c2*), C03_DC (*H2-Eb1*, *H2-Aa*), C04_T (*Ccl5*, *Trbc2*), C05_Neu (*S100a8*, *S100a9*), C06_Endo (*Cdh5*, *Fabp4*), C07_Smooth_Muscle (*Myl9*), C08_Mesenchymal_Pro (*Acta2*, *Myh11*), C09_Teno/FAP (*Dcn*, *Col1a1*), C10_MuSC (*Pax7*, *Gpx3*), and C11_Mature_SM (*Tnnt3*, *Tnnc2*). For 11,12-EET treatment analysis, C01_Mono/Mac (*C1qc*, *C1qb*), C02_DC (*H2-Eb1*, *H2-Aa*), C03_T (*Ccl5*, *Trbc2*), C04_Neu (*S100a8*, *S100a9*), C05_Endo (*Cdh5*, *Fabp4*), C06_Smooth_Muscle (*Myl9*), C07_Teno/FAP (*Dcn*, *Col1a1*), C08_MuSC (*Pax7*, *Gpx3*), C09_Mature_SM (*Tnnt3*, *Tnnc2*), and C10_Peripheral_nerves (*Mpz*, *Kcna1*).

For VISION analysis⁵⁴, GO terms were curated from mouse-native gene sets of MsigDB⁵⁵. Signature scores were calculated with the getSignatureScores function of VISION (v2.1.0). Signature autocorrelations were evaluated with a Geary's C method and the enrichment results

were add back to Seurat data. For the determination of highly dynamic immune cell types, inflammatory index and regeneration index were determined by the VISION-enriched score of 'GOBP_ACUTE_INFLAMMATORY_RESPONSE' and 'GOBP_MUSCLE_ORGAN_DEVELOPMENT', respectively. ANOVA test between these two indexes with time was performed, and $P < 1 \times 10^{-30}$ was used as a cut-off. Other enrichment analysis was based on AddModuleScore with indicated gene sets curated from MsigDB. Correlation between FGF signalling was performed between each gene and 'GOBP_RESPONSE_TO_FIBROBLAST_GROWTH_FACTOR' score, and top 300 genes were used for ClusterProfiler (v4) GO enrichment. Correlation level was plotted using ggstatplot (v0.12.0). For trajectory analysis, CytoTRACE score was calculated with CytoTRACE (v0.3.3) with default setting⁵⁶. Monocle3 (v1.2.9) was used for lineage analysis, and Proliferating lineage and Differentiation lineage were determined using order_cells function after setting *Pax7*^{high} cells as start point. For cell-cell interaction analysis, we performed NicheNet⁵⁷ analysis using subset of day 2 scRNA-seq data (WT_Day2 and KO_Day2). All cell types were used as receiver and sender, and top 15 enriched ligands were calculated.

OLINK analysis

After collection of muscle TIF, the proteins were measured using the Olink Target 96 Mouse Exploratory Panel (Olink Proteomics) according to the manufacturer's instructions. The proximity extension assay technology used for the Olink protocol has been described⁵⁸. In brief, proximity-dependent DNA polymerization generates a unique PCR target sequence. The resulting DNA sequence is subsequently detected and quantified using a microfluidic real-time PCR instrument (Biomark HD, Fluidigm). Data are then quality controlled and normalized using an internal extension control and an inter-plate control, to adjust for intra- and inter-run variation. The final assay read-out is presented in normalized protein expression (NPX) values, which are in arbitrary units on a log₂ scale, where a high value corresponds to a higher protein expression. All assay validation data (such as detection limits, intra- and inter-assay precision data) are available on the manufacturer's website.

Untargeted metabolomics

Sample extraction. For the extraction of hydrophilic compounds, samples were thawed on ice, and 3 volumes of ice-cold methanol to 1 volume of supernatants or TIF were added, followed by spinning the mixture for 3 min and centrifugation at 12,000 rpm for 10 min at 4 °C. Centrifugation was repeated, and the supernatant used for LC-MS/MS analysis. For the extraction of hydrophobic compounds, samples were thawed on ice, and spun for 10 s. Samples were then centrifuged at 3,000 rpm for 5 min at 4 °C. Fifty microlitres of sample was homogenized with 1 ml mixture (methanol, methyl *tert*-butyl ether, and internal standard mixture). The mixture was spun for 2 min, followed by addition of 500 µl of water and spinning for another 1 min. The mixture was centrifuge at 12,000 rpm for 10 min at 4 °C, and 500 µl extract was lyophilized. The powder was dissolved with 100 µl mobile phase B, and then added into the sample bottle for LC-MS/MS analysis.

UPLC conditions. For hydrophilic compounds, the sample extracts were analysed using an LC-ESI-MS/MS system (UPLC, Shim-pack UFLC Shimadzu CBM A system; MS, Q TRAP System). The analytical conditions were as follows, UPLC: column, Waters Acquity UPLC HSS T3 C18 (1.8 µm, 2.1 mm × 100 mm); column temperature, 40 °C; flow rate, 0.4 ml min⁻¹; injection volume, 2 µl; solvent system, water (0.1% formic acid): acetonitrile (0.1% formic acid); gradient program, 95:5 v/v at 0 min, 10:90 v/v at 11.0 min, 10:90 v/v at 12.0 min, 95:5 v/v at 12.1 min, 95:5 v/v at 14.0 min. For hydrophobic compounds, the analytical conditions were as follows, UPLC: column, Thermo C30 (2.6 µm, 2.1 mm × 100 mm); solvent system, A: acetonitrile/water (60/40 v/v, 0.04% acetic acid, 5 mmol l⁻¹ammonium formate), B: acetonitrile/isopropanol

(10/90 v/v, 0.04% acetic acid, 5 mmol l⁻¹ammonium formate); gradient program, A/B (80:20 v/v) at 0 min, 50:50 v/v at 3.0 min, 35:65 v/v at 5 min, 25:75 v/v at 9 min, 10:90 v/v at 15.5 min; flow rate, 0.35 ml min⁻¹; temperature, 45 °C; injection volume: 2 µl. The effluent was connected to an ESI-triple quadrupole-linear ion trap (Q TRAP) mass spectrometer.

ESI-Q TRAP-MS/MS settings. For hydrophilic compounds, linear ion trap (LIT) and QQQ scans were acquired on a Q TRAP LC-MS/MS system, equipped with an ESI Turbo Ion-Spray interface, operating in positive and negative ion mode and controlled by Analyst 1.6.3 software (Sciex). The ESI source operation parameters were as follows: source temperature 500 °C; IS, 5,500 V (positive), -4,500 V (negative); GSI, GSII, and CUR were set at 55, 60, and 25.0 psi, respectively; the CAD was high. Instrument tuning and mass calibration were performed with 10 and 100 µmol l⁻¹ polypropylene glycol solutions in QQQ and LIT modes, respectively. A specific set of multiple reaction monitoring (MRM) transitions were monitored for each period according to the metabolites eluted within this period. For hydrophobic compounds, the ESI source operating parameters were as follows: ion source, turbo spray; source temperature 550 °C; IS, 5,500 V; GSI, GSII, and CUR were set at 55, 60, and 25 psi, respectively; the CAD was medium. Instrument tuning and mass calibration were performed with 10 and 100 µmol l⁻¹ polypropylene glycol solutions in QQQ and LIT modes, respectively. QQQ scans were acquired as MRM experiments with collision gas (nitrogen) set to 5 psi. Declustering potentials (DP) and collision energies (CE) for individual MRM transitions were done with further DP and CE optimization. A specific set of MRM transitions was monitored for each period according to the metabolites eluted within this period. Metabolomics was performed with the assistance of MetWare, Wuhan. Fold change of metabolites level in Fig. 3 and Extended Data Fig. 5 was determined by Limma package (version 3.54.0) unless otherwise noted.

For LC-MS/MS detection of 11,12-EET in TIF, TIF was isolated from CTX-injected muscles of both *Gsdmd*^{f/f} and *Gsdmd*^{f/f}-*Lyz2-cre* mice. TIFs were extracted with 550 µl ice methanol, containing 10 mM butylhydroxytoluene, 10 µl formic acid, and internal standard (carnitine C2:0-d3:0.08 µg ml⁻¹; carnitine C8:0-d3: 0.05 µg ml⁻¹; carnitine C10:0-d3:0.05 µg ml⁻¹; carnitine C16:0-d3: 0.08 µg ml⁻¹; lysophosphatidylcholine 19:0:0.38 µg ml⁻¹; free fatty acid (FFA) C16:0-d3: 1.25 µg ml⁻¹; FFA C18:0-d3: 1.25 µg ml⁻¹; goose deoxycholic acid-d4: 0.75 µg ml⁻¹; cholic acid-d4: 0.93 µg ml⁻¹; Trp-d5: 2.13 µg ml⁻¹; Phe-d5: 1.80 µg ml⁻¹; sphingomyelin 12:0:0.38 µg ml⁻¹; choline-d4: 1.00 µg ml⁻¹). Solutions were sonicated on ice with 60 cycles (working time 3 s and pause time 2 s, 400 W). After centrifugation at 15,000 rpm (4 °C) for 20 min, the supernatants were transferred to another Eppendorf tube. After adding 700 µl H₂O and 1 ml ethyl acetate, the supernatants were vortexed for 30 s on ice, followed by centrifugation at 12,000 rpm (4 °C) for 10 min. The organic phase was isolated, and the aqueous phase was extracted for another round. The collected organic phase was lyophilized and dissolved in 100 µl methanol for LC-MS/MS detection. Following LC-MS/MS detection was performed with the assistance of Dalian ChemDataSolution Information Technology.

Targeted oxylipin metabolomics

All eicosanoids and deuterated internal standards were purchased from Cayman Chemical. The stock solutions of standards were prepared at the concentration of 0.1 mg ml⁻¹ in methanol. All stock solutions were stored at -20 °C. The stock solutions were diluted with methanol to working solutions before analysis.

Sample preparation and extraction. For the analysis of cell samples, 10⁷ macrophages were spiked with 200 µl of oxidized lipid extract, vortexed for 5 min, and the protein was precipitated at low temperature (~20 °C). For supernatants, aliquots of 100 µl were spiked with 200 µl of oxidized lipid extract, vortexed for 5 min, and the protein was

Article

precipitated at low temperature (-20°C). Samples were then spiked with 20 μl of 1 μM internal standard mixture to each sample and vortexed for 10 min, then centrifuged at 5,000 rpm for 10 min at 4°C . The extraction step was repeated and the supernatants were combined. The eicosanoids in supernatants were extracted using Poly-Sery MAX SPE columns (ANPEL). Prior to analysis, the eluent was dried under vacuum and re-dissolved in 100 μl of methanol/water (1:1, v/v) for UPLC/MS–MS analysis.

HPLC conditions. The sample extracts were analysed using an LC-ESI-MS/MS system (UPLC, ExionLC AD; MS, Q TRAP 6500+ System). The analytical conditions were as follows, HPLC: column, Waters Acuity UPLC HSS T3 C18 (100 mm \times 2.1 mm i.d., 1.8 μm); solvent system, water with 0.04% acetic acid (A), acetonitrile with 0.04% acetic acid (B); the gradient was 0–2.0 min from 0.1% to 30% B; 2.0–4.0 min to 50% B; 4.0–5.5 min to 99% B, which was maintained for 1.5 min; and 6.0–7.0 min reduced to 0.1% B and maintained for 3.0 min; flow rate, 0.4 ml min $^{-1}$; temperature, 40 $^{\circ}\text{C}$; injection volume: 10 μl .

ESI-MS/MS conditions. LIT and QQQ scans were acquired on Q TRAP 6500+ LC–MS/MS System, equipped with an ESI Turbo Ion-Spray interface, operating in negative ion mode and controlled by Analyst 1.6.3 software (Sciex). The ESI source operation parameters were as follows: ion source, turbo spray; source temperature 550 $^{\circ}\text{C}$; IS –4,500 V; CUR was set at 35 psi. Eicosanoids were analysed using scheduled MRM. Data were acquired using Analyst 1.6.3 software (Sciex). Multiquant software (Sciex) was used to quantify all metabolites. Mass spectrometer parameters including the DP and CE for individual MRM transitions were done with further DP and CE optimization. A specific set of MRM transitions was monitored for each period according to the metabolites eluted within this period. Eicosanoids contents were detected by MetWare based on the AB Sciex Q TRAP 6500 LC–MS/MS platform.

Quantification and statistical analysis

Statistical analyses were performed with Prism software (GraphPad 9) or R. Rstudio (version 2022.07.2 + 576) and JupyterLab (version 4.0.7) are used for coding. Statistical significance was evaluated with the two-tailed unpaired Student's *t*-test for comparing two groups, the two-tailed paired Student's *t*-test for paired group comparisons, one-way ANOVA for comparing more than two groups, two-way ANOVA for CSA analysis, and the Wilcoxon rank sum test for scRNA-seq data as indicated. Correction methods are indicated in the figure legend. * $P < 0.05$, ** $P < 0.01$, *** $P < 0.001$, **** $P < 0.0001$; NS, not significantly different. Box plots show the entire range of values, median and quartiles.

Reporting summary

Further information on research design is available in the Nature Portfolio Reporting Summary linked to this article.

Data availability

All raw and processed sequencing data generated in this study have been deposited in the NCBI Gene Expression Omnibus (GEO) under accession numbers GSE246007 (bulk RNA sequencing) and GSE250049 (scRNA-seq). The publicly available dataset used in this study is available at GEO under the accession numbers GSE113631 and GSE164471. The gating strategy for flow cytometry and raw, uncropped images of western blots are provided in the Supplementary Information. Source data are provided with this paper.

48. Liu, L., Cheung, T. H., Charville, G. W. & Rando, T. A. Isolation of skeletal muscle stem cells by fluorescence-activated cell sorting. *Nat. Protoc.* **10**, 1612–1624 (2015).
49. Hoeffel, G. et al. Sensory neuron-derived TAFA4 promotes macrophage tissue repair functions. *Nature* **594**, 94–99 (2021).
50. Rowland, M. B., Moore, P. E., Bui, C. & Correll, R. N. Assessing wound closure in mice using skin-punch biopsy. *STAR Protoc.* **4**, 101989 (2023).
51. Chi, Z. et al. Histone deacetylase 3 couples mitochondria to drive IL-1 β -dependent inflammation by configuring fatty acid oxidation. *Mol. Cell* **80**, 43–58.e47 (2020).
52. Wu, T. et al. clusterProfiler 4.0: a universal enrichment tool for interpreting omics data. *Innovation* **2**, 100141 (2021).
53. Hao, Y. et al. Integrated analysis of multimodal single-cell data. *Cell* **184**, 3573–3587.e3529 (2021).
54. DeTomaso, D. et al. Functional interpretation of single cell similarity maps. *Nat. Commun.* **10**, 4376 (2019).
55. Castanza, A. S. et al. Extending support for mouse data in the Molecular Signatures Database (MSigDB). *Nat. Methods* **20**, 1619–1620 (2023).
56. Gulati, G. S. et al. Single-cell transcriptional diversity is a hallmark of developmental potential. *Science* **367**, 405–411 (2020).
57. Browaeys, R., Saelens, W. & Saeyns, Y. NicheNet: modeling intercellular communication by linking ligands to target genes. *Nat. Methods* **17**, 159–162 (2020).
58. Assarsson, E. et al. Homogenous 96-plex PEA immunoassay exhibiting high sensitivity, specificity, and excellent scalability. *PLoS ONE* **9**, e95192 (2014).

Acknowledgements The authors thank I. C. Bruce for reading the manuscript; Z. Zhao for support with flow cytometric experiments; S.-Z. Luo for providing eGFP–bFGF plasmids; X. Gao and S. Xu for support with phase separation experiments; and Q. Han for technical support. This work was supported by the National Natural Science Foundation of China (82025017 and 81930042 to D.W., 32370919 and 32100692 to Z.C. and 32370832 to W.Y.), the China Postdoctoral Science Foundation (2023M733063 to Z.W.), the Huadong Medicine Joint Funds of the Zhejiang Provincial Natural Science Foundation of China (LHMD23H160002 to D.W.), the Key R&D Program of Zhejiang (2024ASSYS0024 to D.W.), and the Dr Li Dak Sum & Yip Yio Chin Development Fund for Regenerative Medicine. Graphics in Figs. 3c, 4i, 5n and 6e,i,n,s and Extended Data Figs. 1a,d,j, 5a,e,f,q and 10a,j were created using BioRender.com.

Author contributions Z.C., S.C., D.Y., W.C., Y. Lu, Z.W., M.L., Y.J., W.Y., J.Z., Q.Y., T.H., X.L., Q.D., Y.Y., T.Z. and M.C. performed animal and cell experiments. S.C. and R.S. performed scRNA-seq downstream analysis. Q.X. and K.D. provided human muscle samples. Z.C., S.C., D.Y., M.L., W.C., Y. Li, M.S., X.Z. and D.W. conceived and designed the study. Z.C., S.C., D.Y. and D.W. wrote the manuscript, and Z.C. and D.W. supervised the project.

Competing interests The authors declare no competing interests.

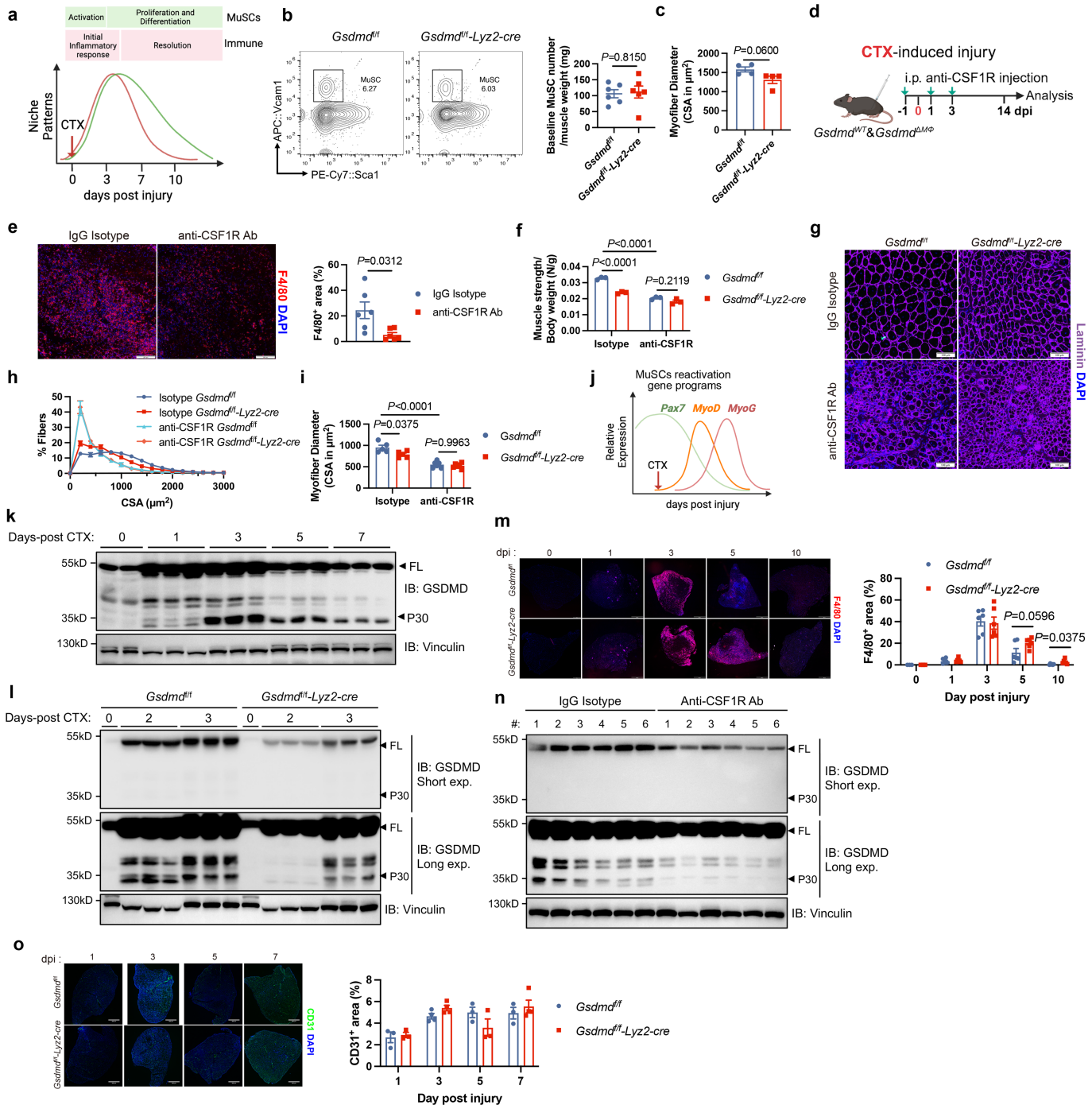
Additional information

Supplementary information The online version contains supplementary material available at <https://doi.org/10.1038/s41586-024-08022-7>.

Correspondence and requests for materials should be addressed to Zhexu Chi or Di Wang.

Peer review information *Nature* thanks the anonymous reviewer(s) for their contribution to the peer review of this work.

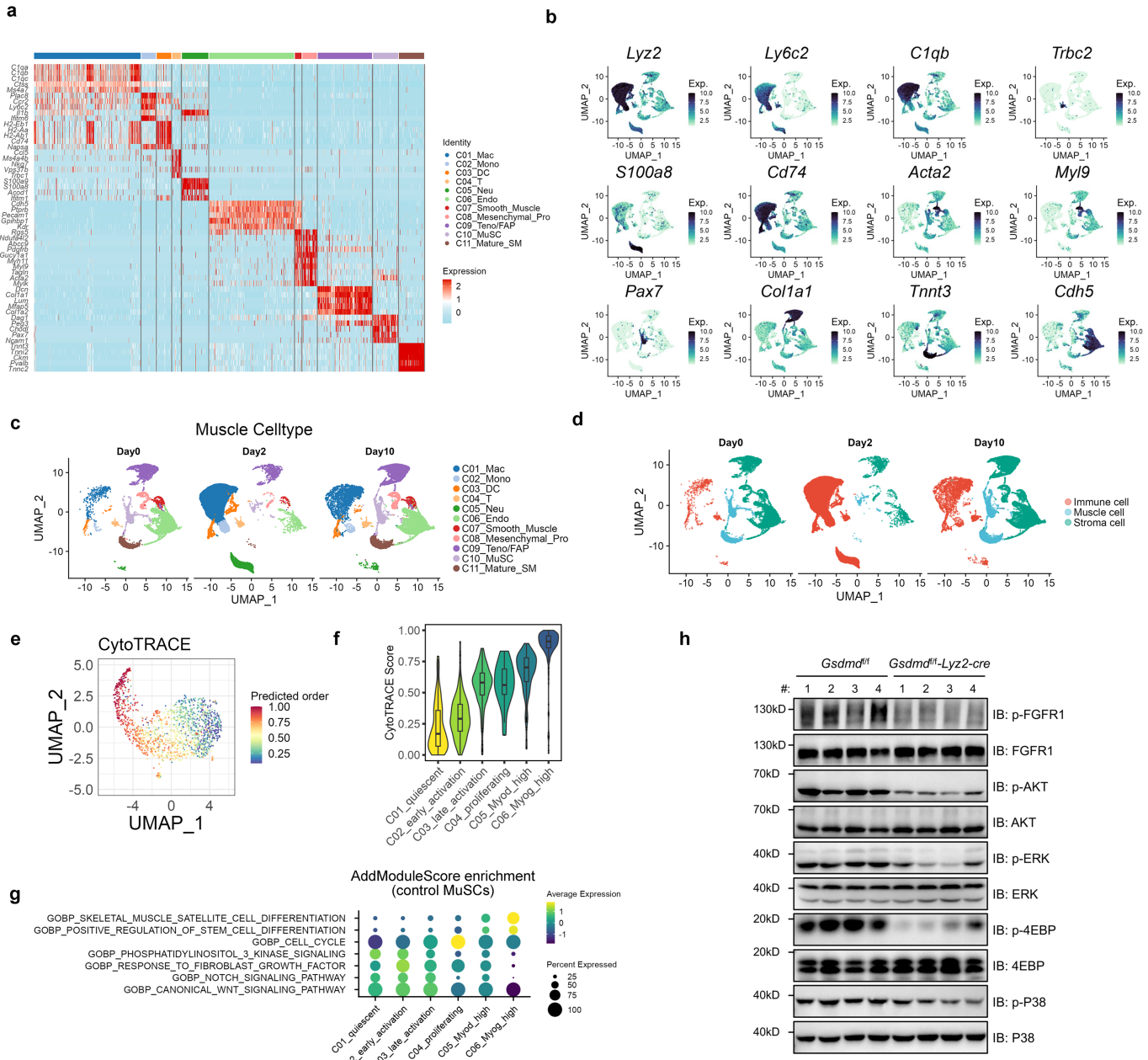
Reprints and permissions information is available at <http://www.nature.com/reprints>.



Extended Data Fig. 1 | Myeloid GSDMD deficiency compromises tissue repair. **a**, Schematic of the tissue repair process coupled with an inflammatory response. **b,c**, Representative flow cytometry analysis contour plots (**b**, left), quantification (**b**, right) of baseline MuSC number and mean CSA (**c**), related to Fig. 1d (n = 4), from tibialis anterior muscles of *Gsdmd*^{fl/fl} and *Gsdmd*^{CKO} mice (n = 6). **d-i**, Schematic of *Gsdmd*^{CKO} and littermate controls subjected to CTX-induced injury upon macrophage depletion by anti-CSF1R antibody intraperitoneally (**d**). Representative images and quantification of macrophages at 3 dpi (**e**). Muscle strength (n = 3) (**f**), myofiber CSA (**g**), frequency distribution (**h**) and mean CSA (**i**) of TA muscles at 14 dpi with isotype or anti-CSF1R injection (n = 5, isotype; n = 6, anti-CSF1R). **j**, Schematic of MuSC

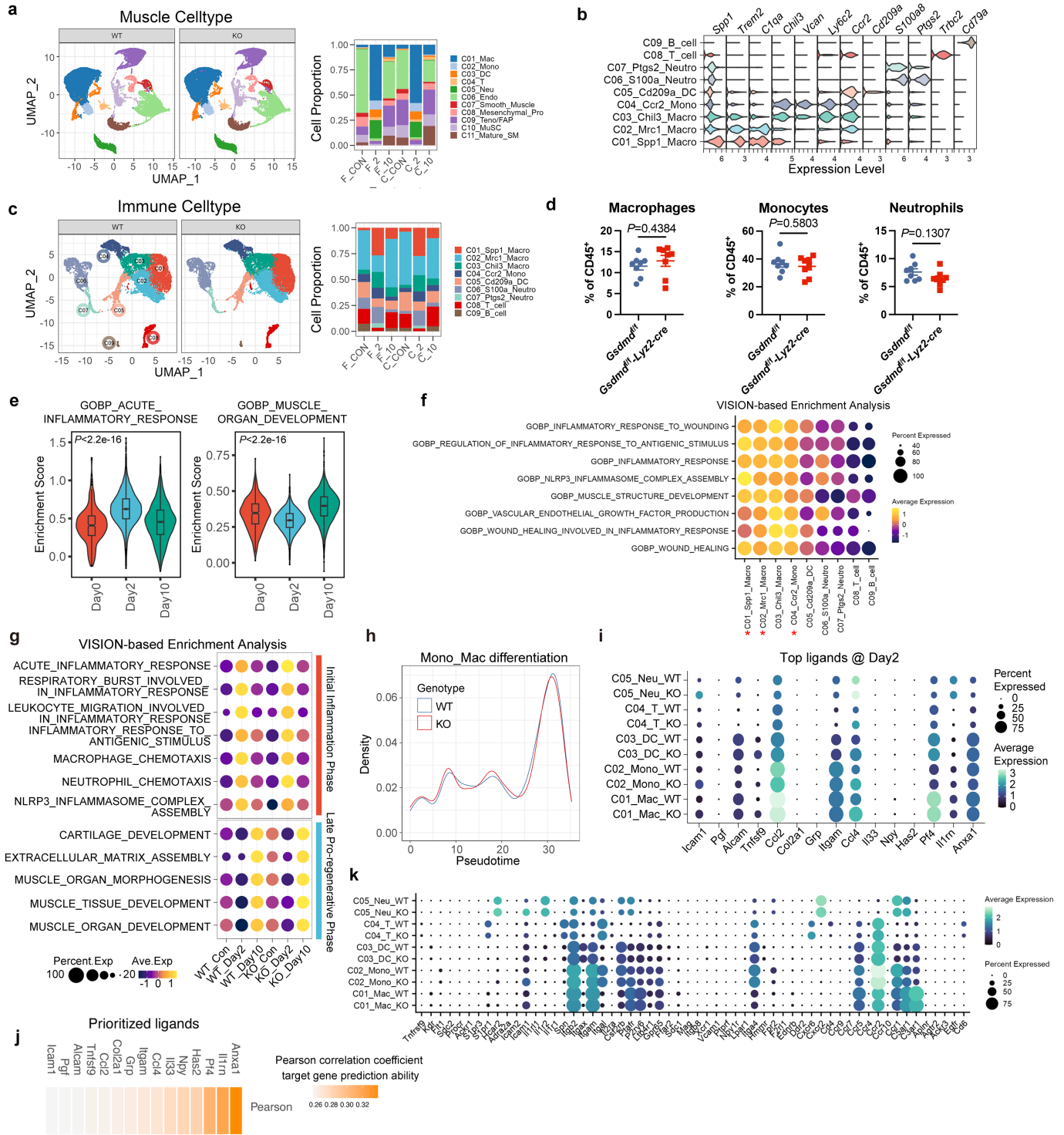
myogenic gene programs during regeneration. **k,l**, Immunoblots of GSDMD in muscle extracts post CTX injury at indicated time. **m**, Representative images and quantitation (n = 3, 0 dpi; n = 6, 1–10 dpi) of F4/80⁺ staining in injured TA muscles. **n**, Immunoblots of muscle extracts for GSDMD from mice with isotype or anti-CSF1R injection at 3 dpi. **o**, Representative images and quantitation (n = 3, 1 dpi; n = 4, 3 dpi; n = 3, 5 dpi; n = 3 *Gsdmd*^{fl/fl}, n = 4 *Gsdmd*^{CKO}, 7 dpi) of CD31⁺ staining in injured TA muscles. A representative (**b,c,e,k-o**) of at least two independent experiments is shown. Unpaired two-tailed t test applied for (**b,c,e,m,o**). Two-way ANOVA applied for (**f,h,i**) with Šidák correction. Mean ± SEM.

Article



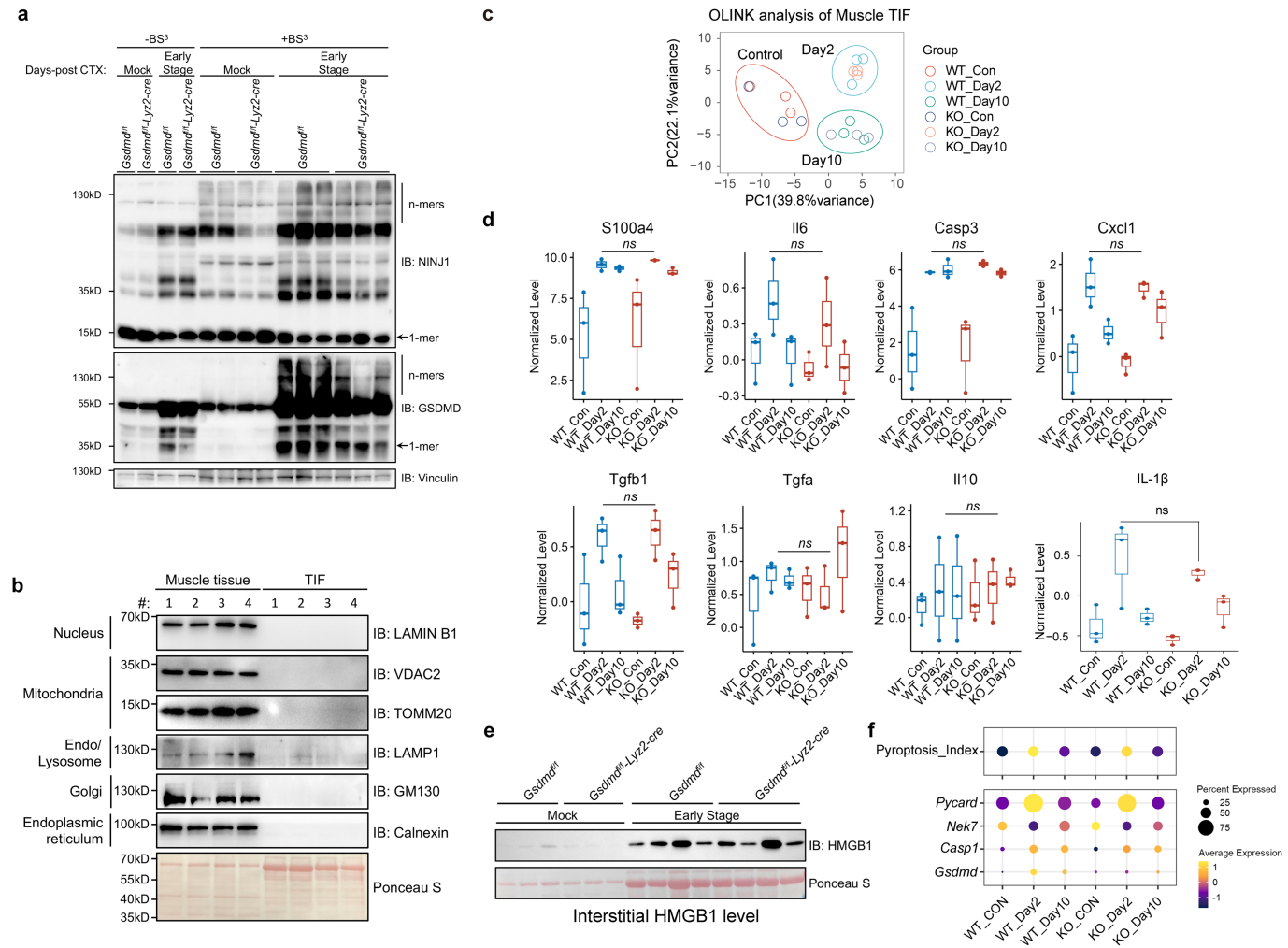
Extended Data Fig. 2 | Single-cell data analysis of muscles from *Gsdmd*^{fl/fl} and *Gsdmd*^{CKO} mice. **a,b**, Heatmap (**a**) and featureplot (**b**) showing the expression of signature markers of each cell type. **c,d**, UMAP plot of dynamics of cell populations during regeneration. **e-f**, CytoTRACE score of each state of MuSCs (**e,f**). Dotplot of the enrichment score of indicated gene sets calculated by

AddModuleScore, related to Fig. 2d (**g**). **h**, Immunoblots and grayscale statistics of the PI3K-AKT-mTOR and MAPK signaling pathways downstream of FGF-FGFR in TA muscles from *Gsdmd*^{fl/fl} and *Gsdmd*^{CKO} mice subjected to CTX-induced injury. A representative (**h**) of at least two independent experiments is shown.



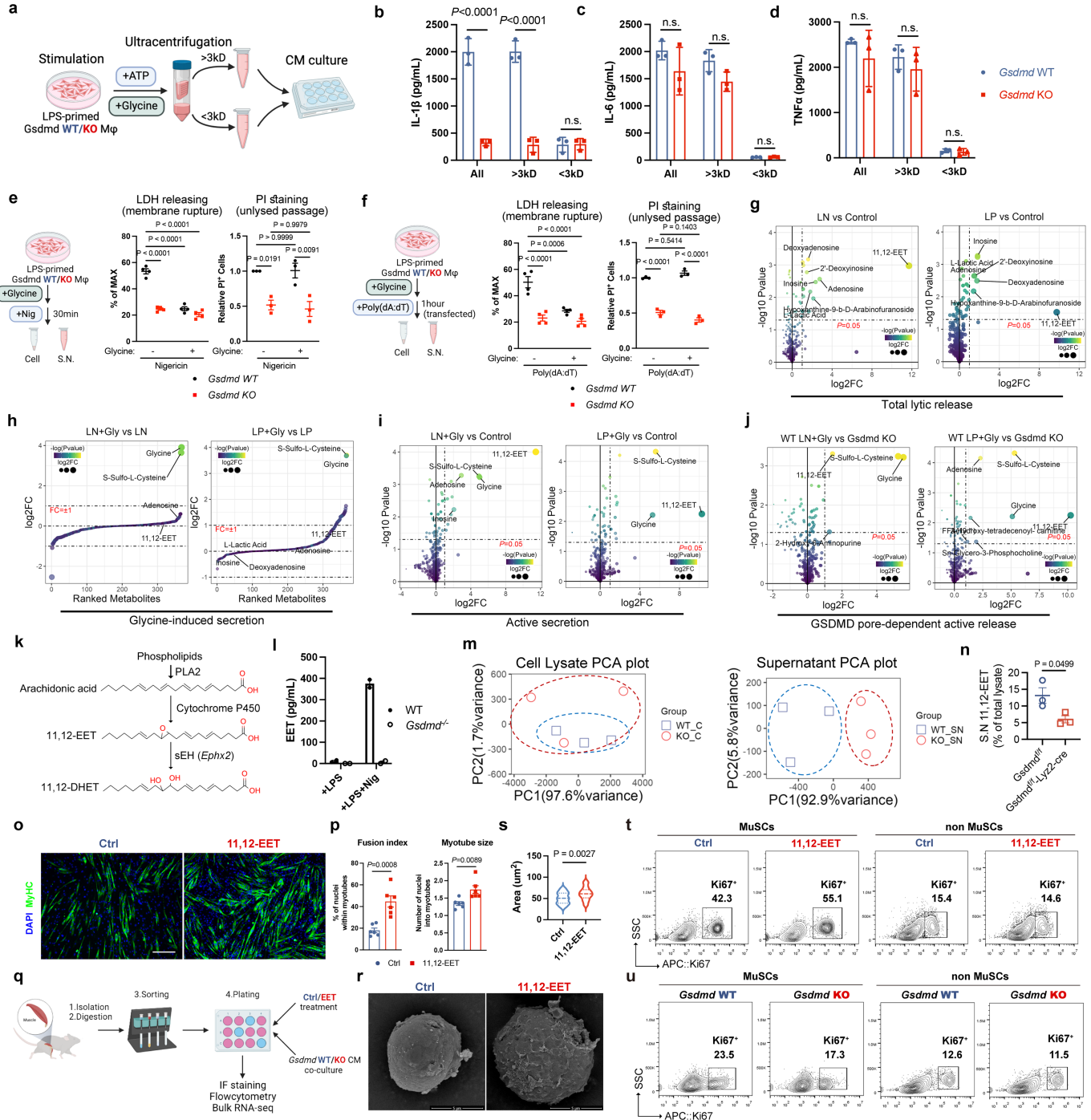
Extended Data Fig. 3 | Single-cell data analysis of intramuscular immune components of *Gsdmd*^{+/+} and *Gsdmd*^{-/-} mice. **a-c**, Analysis of intramuscular immune components of *Gsdmd*^{+/+} and *Gsdmd*^{-/-} mice. Dynamics of percentages of each cell type in *Gsdmd*^{+/+} and *Gsdmd*^{-/-} muscles (**a**). Stacked violin plot of signature marker genes of each immune cell type (**b**) and dynamics of immune cell percentages in *Gsdmd*^{+/+} and *Gsdmd*^{-/-} muscles (**c**). **d**, Flow cytometry analysis of myeloid cell composition at 2 dpi (n = 8). **e,f**, Violin plot (**e**) and dotplot of VISION enrichment analysis of indicated signature genesets (**f**).

g, Dotplot of the enrichment score of indicated gene sets in highly dynamic immune cells determined in *Ccr2*^{high} monocytes, *Spp1*^{high} and *Mrc1*^{high} macrophages. **h**, Trajectory analysis of the monocyte-macrophage lineage. **i**, Expression of the top ranked ligands in immune cells upon injury. **j,k**, Cell-cell interaction analysis using NicheNet. Top ranked intramuscular ligands at 2 dpi (**j**) and expression of top ranked receptors in each immune cell type (**k**). A representative of at least two independent experiments is shown. Unpaired two-tailed t test applied for (**d**). Mean ± SEM.



Extended Data Fig. 4 | *Gsdmd* deficiency has little impact on the muscle microenvironment upon injury. **a**, Immunoblots of GSDMD and NINJ1 oligomerization (a) in injured TA muscle lysates (2dpi) after treatment with/without the membrane-impermeable BS³ crosslinker, which stabilizes protein-protein interactions for further analysis by immunoprecipitation. The intensity of Vinculin was used as control. **b**, Immunoblots of intracellular proteins using total muscle lysates and TIF to confirm the purity of the interstitial fluid. Ponceau S is used as loading control. **c**, OLINK analysis of

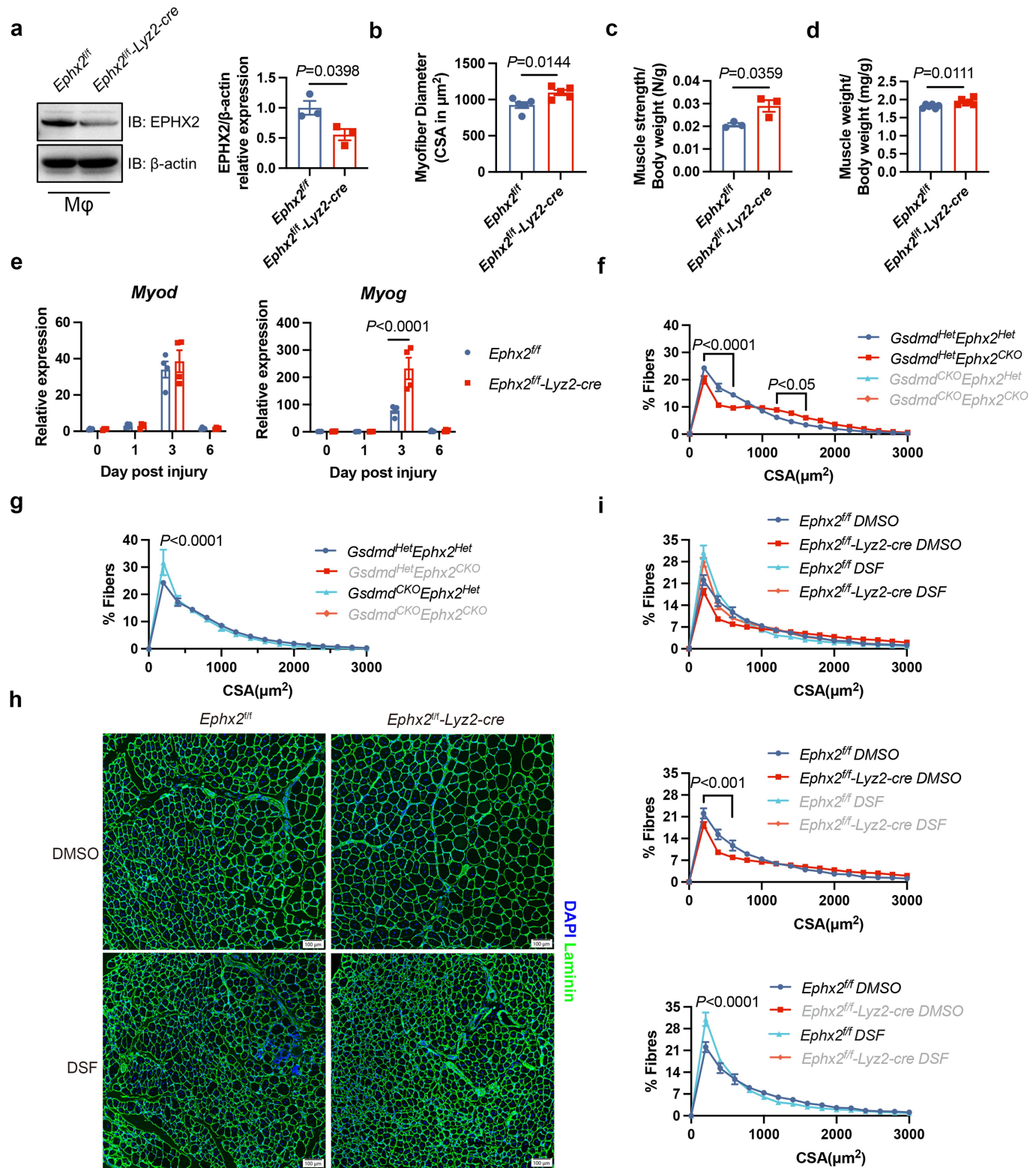
muscle TIF. PCA plot of each sample during regeneration. **d**, Intramuscular levels of inflammatory and regenerating proteins determined by OLINK ($n = 3$ per group), and boxchart of intramuscular IL1 β protein levels ($n = 3$). **e**, Immunoblots of HMGB1 secretion in muscle TIF at 2 dpi. **f**, Dotplot of pyroptosis index and indicated gene expression of three highly dynamic immune cell types. A representative (a,b,e) of at least two independent experiments is shown. Unpaired two-tailed t test applied for (d). Abbreviation: BS³, bis-(sulfosuccinimidyl)-suberate, used as a crosslinker.



Extended Data Fig. 5 | Release of GSDMD-dependent metabolites promotes tissue regeneration. **a**, Schematic of supernatant collection and ultracentrifugation. Macrophages were stimulated with 500 ng/mL LPS for 4 h. Thirty minutes before the second signal (3.5 h post LPS stimulation), 10 mM glycine was supplemented to maintain plasma membrane integrity. The second signals, 10 μM nigericin or 1 μg/mL poly(dA:dT), were added to induce GSDMD pore formation. **b-d**, Quantification of IL-1β (**b**), IL-6 (**c**) and TNFα (**d**) by ELISA (n = 3). **e,f**, LDH levels in supernatants determined by LDH releasing assay (n = 4) and PI⁺ cells detected by flow cytometry (n = 3). **g-j**, Volcano plot of metabolite levels with indicated comparisons, representing total lytic release (**g**), glycine-induced secretion (**h**), active secretion (**i**), and GSDMD pore-dependent active release (**j**), related to Fig. 3c,d,k. **k**, Schematic of 11,12-EET biogenesis and hydrolysis. **l**, 11,12-EET levels in supernatants determined by

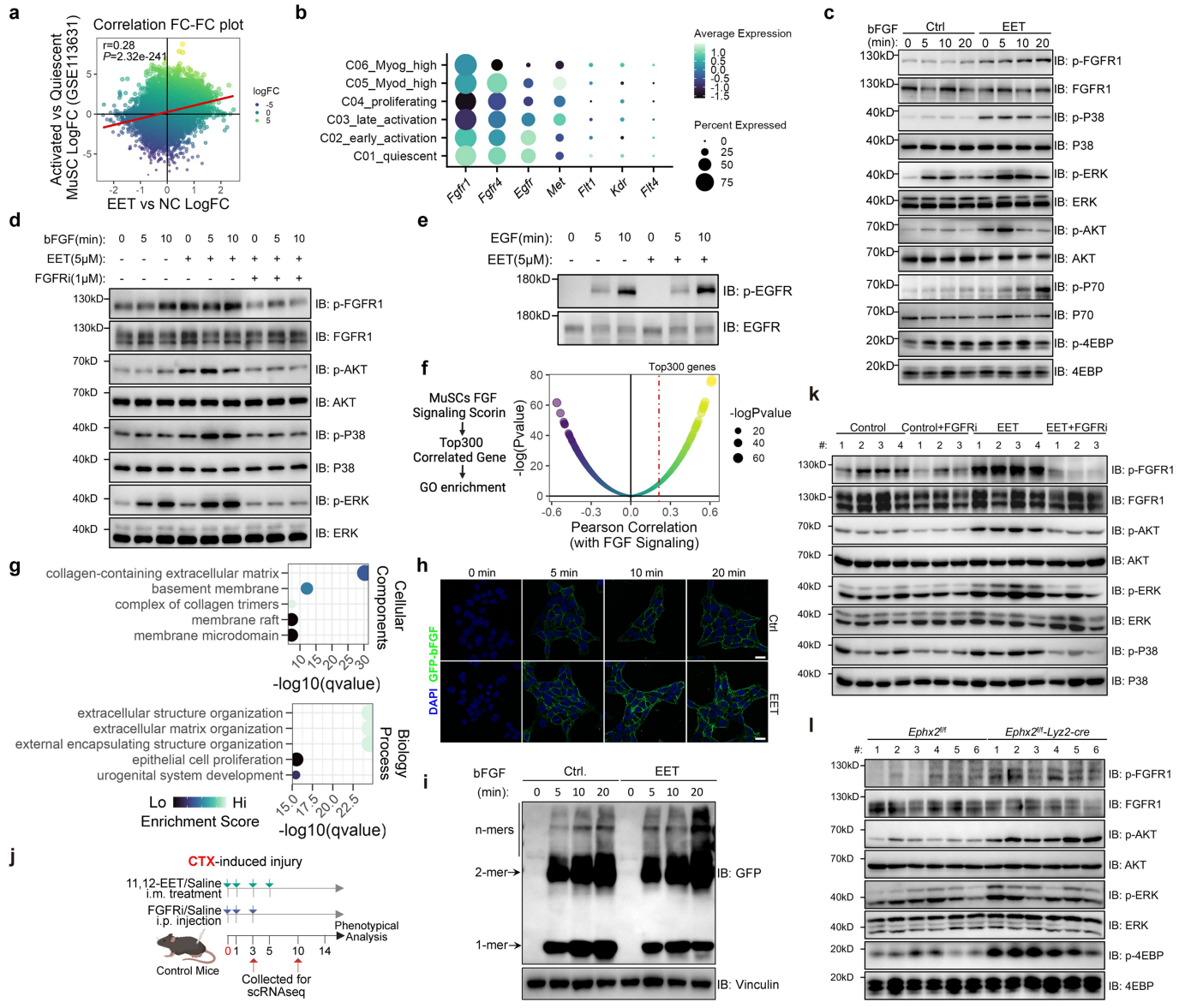
ELISA (n = 2, technical replicates). **m**, PCA plot of targeted metabolites of cell lysates and supernatants, related to Fig. 3e. **n**, The proportion of 11,12-EET secretion in the supernatant relative to the intracellular quantity, related to Fig. 3e. **o,p**, Representative images (**o**) and quantification (**p**) of C2C12 cell fusion index and myotube size with/without 11,12-EET treatment (n = 6). Scale bar, 200 μm. **q**, Schematic of primary MuSC isolation procedure (**r,s**). **r,s**, Representative scanning electron microscope image (**r**) and statistics (**s**) of 11,12-EET treated (n = 30) and control (n = 40) MuSCs. **t,u**, Representative flow cytometry contour plots, related to Fig 1, m. A representative (**l,o,p,r**) or a pool (**b,f,s-u**) of at least two independent experiments is shown. Unpaired two-tailed t test applied for (**b-d,n,p,s**). Two-way ANOVA applied for (**e,f**) with Šidák correction. Mean ± SEM, except Mean ± SD for **51**.

Article



Extended Data Fig. 6 | Accumulation of 11,12-EET boosts tissue regeneration in vivo. **a**, Immunoblots and quantification ($n = 3$) of EPHX2 expression in peritoneal macrophages. **b**, Mean CSA ($n = 5$), related to Fig. 4c. **c,d**, Muscle strength ($n = 3$) (c) and weight ($n = 6$) (d) of TA muscles from *Ephx2^{ff}* and *Ephx2^{CKO}* mice at 14 dpi. **e**, Expression of *Myod* and *Myog* mRNA levels in *Ephx2^{ff}* and *Ephx2^{CKO}* muscle at indicated dpi ($n = 4$). **f,g**, The frequency distribution ($n = 3$, *Gsdmd^{CKO}Ephx2^{CKO}* and *Gsdmd^{ff}Ephx2^{ff}*;

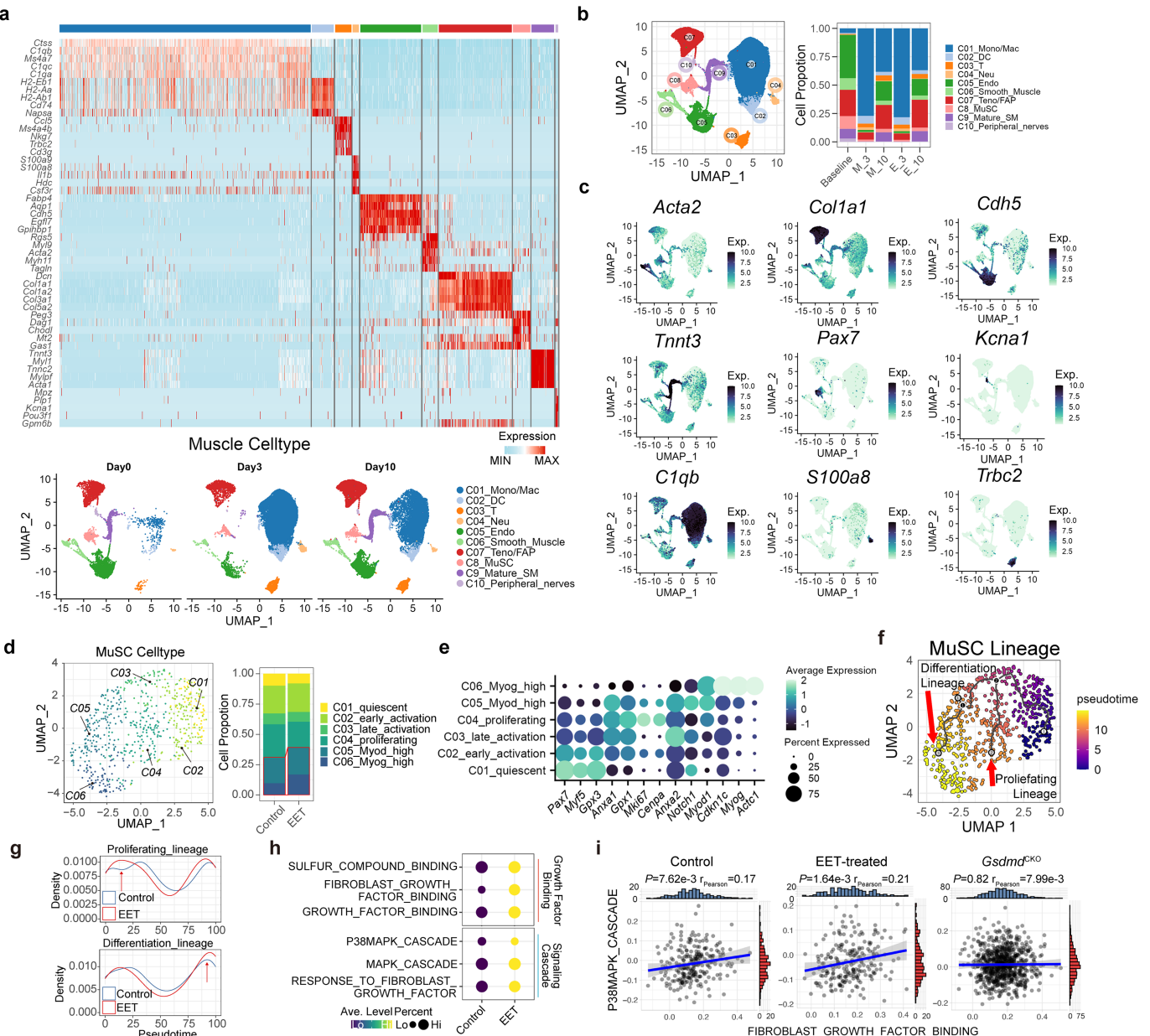
$n = 6$, *Gsdmd^{ff}Ephx2^{CKO}* and *Gsdmd^{ff}Ephx2^{ff}*) of myofiber CSA at 14 dpi, related to Fig. 4j. **h,i**, Representative images of *Ephx2^{ff}* and *Ephx2^{CKO}* TA muscle cross-sections (h) and the frequency distribution ($n = 4$, DMSO; $n = 6$, DSF) (i) of myofiber CSA at 14 dpi with or without DSF treatment. A representative of at least two independent experiments is shown. Unpaired two-tailed t test applied for (a-d); Two-way ANOVA applied for (e-g,i) with Šidák correction. Mean \pm SEM. Abbreviation: DSF, disulfiram (MCE, HY-B0240).



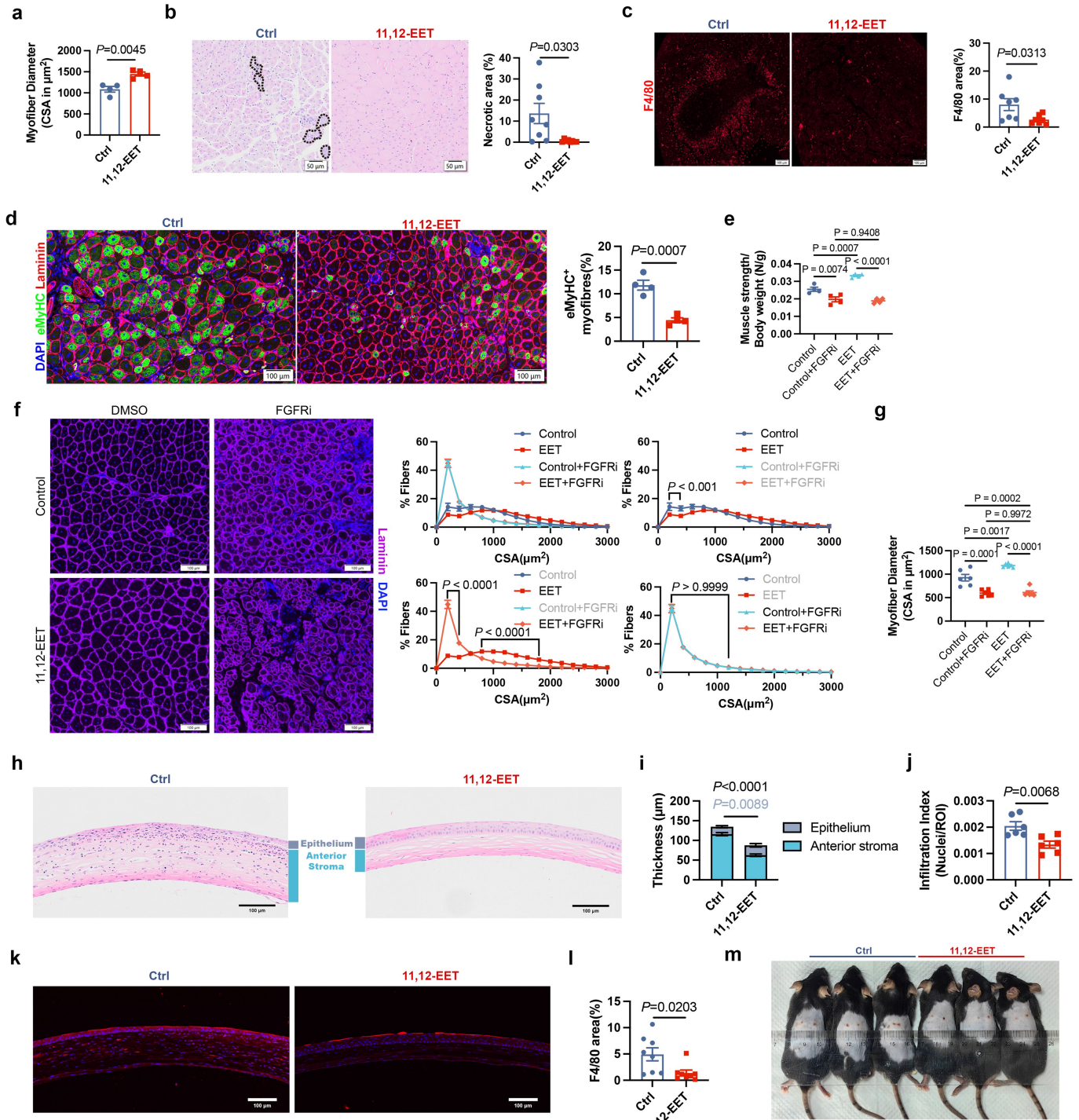
Extended Data Fig. 7 | 11,12-EET propels MuSC proliferation via enhancing FGF-FGFR signalling. **a**, Correlation between gene fold-changes of 11,12-EET *versus* control, and gene fold-changes of activated *versus* quiescent MuSCs (from GSE113631). **b**, Dotplot of expressions of growth factor receptor genes in different MuSC celltype from scRNASeq data of Fig. 2b. **c,d**, Immunoblots of the PI3K-AKT-mTOR and MAPK signalling pathways downstream of FGF-FGFR in NIH-3T3 cells treated with bFGF with/without 11,12-EET (**c**), or with vehicle, 11,12-EET or 11,12-EET + FGFR inhibitor (**d**). **e**, Immunoblots of EGFR activation in NIH-3T3 with or without 11,12-EET. **f,g**, Analysis pipeline of the correlation level between each gene and FGF signalling score (**f**) and GO enrichment with the top 300 correlated genes (**g**), related to Fig. 5d. FGF signalling score was

determined using *AddModuleScore* with gene set ‘RESPONSE_TO_FIBROBLAST_GROWTH_FACTOR’. **h**, Representative images of FGF condensates on cell surface. Scale bars, 10 μm. **i**, Immunoblots of eGFP-bFGF oligomerization in NIH-3T3 cells after FGF treatment with/without 11,12-EET. **j**, Schematic of 11,12-EET treatment and scRNAseq design. **k,l**, Immunoblots of the PI3K-AKT-mTOR and MAPK signalling pathways downstream of FGF-FGFR in TA muscles subjected to CTX-induced injury with vehicle, vehicle+FGFR inhibitor, 11,12-EET or 11,12-EET + FGFR inhibitor intramuscularly treatment (**k**), or from *Ephx2*^{fl/fl} and *Ephx2*^{fl/fl}-*Lyz2-cre* mice at 3 dpi (**l**). A representative (**c-e,h,i,k,l**) of at least two independent experiments is shown. Pearson correlation analysis for (**a**). Abbreviation: FGFRi, FGFR inhibitor.

Article



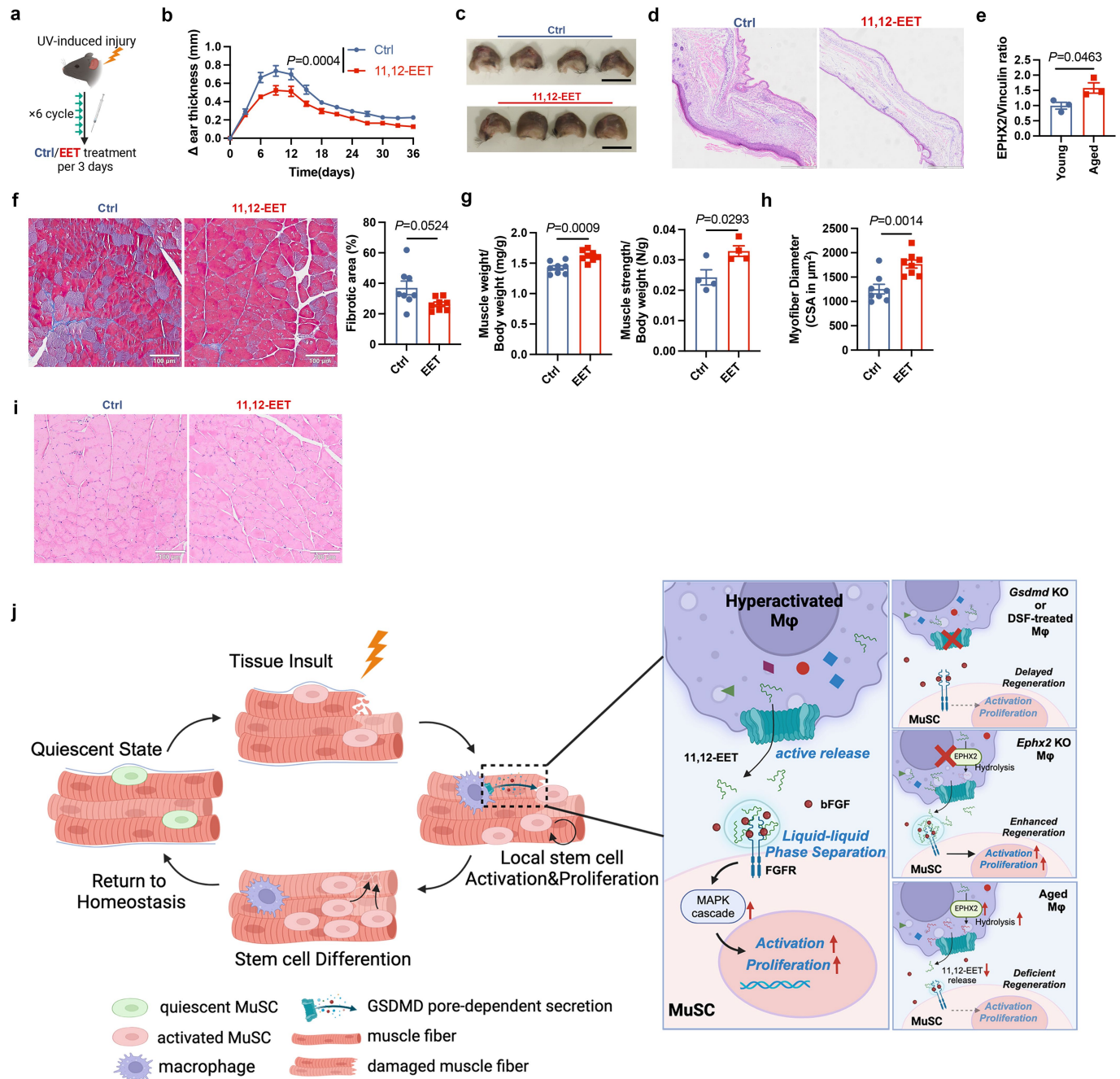
Extended Data Fig. 8 | scRNASeq analysis of muscles with or without 11,12-EET treatment. **a-i**, Heatmap of signature marker genes of each cell type (**a**, upper), and dynamics of cell type population after injury (**a**, lower). UMAP plot and percentage of each cell type with indicated treatment (**b**). Feature plot of signature marker genes of each cell type (**c**). UMAP plot of 6 consecutive MuSC states and changes of cell proportion upon 11,12-EET treatment (**d**). Dotplot of signature marker genes of each state of MuSCs (**e**). Trajectory



Extended Data Fig. 9 | 11,12-EET has multi-organ pro-regenerating capacity. **a**, Mean CSA (n = 4), related to Fig. 6b. **b**, Representative H&E staining of TA muscle cross-sections with/without 11,12-EET supplement and the percentage of necrotic area at 14 dpi (n = 8). **c**, F4/80 immunofluorescence and statistics at 10 dpi (n = 7). **d**, Representative images of eMyHC⁺ myofibers and quantification (n = 4). **e**, The strength (n = 4) of TA muscles with indicated treatment post CTX-induced injury. **f,g**, Representative images (f left panel), the frequency distribution (f right panel) and mean of myofiber CSA (g) at 14 dpi with vehicle, vehicle+FGFR inhibitor, 11,12-EET or 11,12-EET + FGFR inhibitor treatment (n = 6). **h-l**, Representative H&E staining of corneal (h), statistics of

epithelium and anterior stroma layer thickness (i) and inflammation infiltration (j) with 11,12-EET (50 ng 11,12-EET, twice daily) or vehicle treatment (n = 6). F4/80 staining (k) and quantification (n = 8) (l). **m**, Images of mice subjected to skin punch biopsy with 11,12-EET (300 ng daily) or vehicle treatment at 7 dpi. A representative of at least two independent experiments is shown. Unpaired two-tailed t test applied for (a-d,i,j,l); One-way ANOVA for (e,g) with Tukey's multiple comparisons test. Two-way ANOVA applied for (f) with Šidák correction. Mean \pm SEM. Abbreviation: FGFRi, FGFR inhibitor; ROI, region of interest.

Article



Extended Data Fig. 10 | 11,12-EET rejuvenates aged muscle. **a-d**, Schematic of UV-induced skin injury model (**a**). Statistics of wound closure over time ($n = 10$) (**b**), and images of mouse ear post UV irradiation with/without 11,12-EET (300 ng daily) treatment ($n = 4$) (**c**). Representative H&E staining of ears 14 days after UV irradiation (**d**). **e**, Quantification of EPHX2 expression in TA muscles from young and aged mice ($n = 3$), related to Fig. 6l. **f**, Micrographs and quantification of collagen deposition in TA muscles of aged mice by Masson's

trichrome staining ($n = 8$). **g**, Quantification of muscle weight ($n = 8$) and strength ($n = 4$) in vehicle- and 11,12-EET-treated aged mice. **h,i**, Representative cross-sections of TA muscles stained with H&E (**h**) and myofiber CSA quantification ($n = 8$) **i**, Working model. A representative (**c-i**) or a pool (**b**) of at least two independent experiments is shown. Unpaired two-tailed t test applied for (**e-h**). Two-way ANOVA applied for (**b**) with Šidák correction; Mean \pm SEM.

Reporting Summary

Nature Portfolio wishes to improve the reproducibility of the work that we publish. This form provides structure for consistency and transparency in reporting. For further information on Nature Portfolio policies, see our [Editorial Policies](#) and the [Editorial Policy Checklist](#).

Statistics

For all statistical analyses, confirm that the following items are present in the figure legend, table legend, main text, or Methods section.

n/a Confirmed

- The exact sample size (n) for each experimental group/condition, given as a discrete number and unit of measurement
- A statement on whether measurements were taken from distinct samples or whether the same sample was measured repeatedly
- The statistical test(s) used AND whether they are one- or two-sided
Only common tests should be described solely by name; describe more complex techniques in the Methods section.
- A description of all covariates tested
- A description of any assumptions or corrections, such as tests of normality and adjustment for multiple comparisons
- A full description of the statistical parameters including central tendency (e.g. means) or other basic estimates (e.g. regression coefficient) AND variation (e.g. standard deviation) or associated estimates of uncertainty (e.g. confidence intervals)
- For null hypothesis testing, the test statistic (e.g. F , t , r) with confidence intervals, effect sizes, degrees of freedom and P value noted
Give P values as exact values whenever suitable.
- For Bayesian analysis, information on the choice of priors and Markov chain Monte Carlo settings
- For hierarchical and complex designs, identification of the appropriate level for tests and full reporting of outcomes
- Estimates of effect sizes (e.g. Cohen's d , Pearson's r), indicating how they were calculated

Our web collection on [statistics for biologists](#) contains articles on many of the points above.

Software and code

Policy information about [availability of computer code](#)

Data collection	Microscopy: Zeiss LSM 800, Olympus VS200; Western Blot: ChemiScope 3300; RT-PCR: LightCycler 480; FACS: ACEA NovoCyte TM, Beckman moflo Astrios EQ, BD Fortessa; Single cell sequencing: 10x Chromium X; LC-MS/MS: ACQUITY UPLC- Triple Quad 6500.
Data analysis	Imaging: FIJI-ImageJ v1.50e; FACS: FlowJo v10; RT-PCR: Lightcycler 480 software version 1.5; Statistics: GraphPad Prism v9; Bioinformation: Limma package version 3.54.0, FastQC v0.12.1, cutadapt version 2.8, DESeq2 1.36.0, ClusterProfiler 4.4.4, ggplot2 3.4.3, Seurat v4.0.1, VISION 3.0.1, ggstatplot v0.12.0, Cytobase v0.3.3, Monocle3 v1.2.9, NicheNet 2.0.4, Rstudio version 2022.07.2+576 and JupyterLab version 4.0.7.

For manuscripts utilizing custom algorithms or software that are central to the research but not yet described in published literature, software must be made available to editors and reviewers. We strongly encourage code deposition in a community repository (e.g. GitHub). See the Nature Portfolio [guidelines for submitting code & software](#) for further information.

Data

Policy information about [availability of data](#)

All manuscripts must include a [data availability statement](#). This statement should provide the following information, where applicable:

- Accession codes, unique identifiers, or web links for publicly available datasets
- A description of any restrictions on data availability
- For clinical datasets or third party data, please ensure that the statement adheres to our [policy](#)

We have included Data availability section in our manuscript, and all GEO accession are public after 28th July, 2024. All raw and processed sequencing data

generated in this study have been deposited in the NCBI GEO (<https://www.ncbi.nlm.nih.gov/geo/>) under accession number GSE246007 (bulk RNAseq) and GSE250049 (scRNAseq). The publicly available dataset used in this study is available at GEO under the accession number GSE113631 and GSE164471.

Research involving human participants, their data, or biological material

Policy information about studies with [human participants or human data](#). See also policy information about [sex, gender \(identity/presentation\), and sexual orientation](#) and [race, ethnicity and racism](#).

Reporting on sex and gender

No sex- or gender-based analysis was performed.

Reporting on race, ethnicity, or other socially relevant groupings

N/A

Population characteristics

Four patients at the Second Affiliation Hospital of Zhejiang University (SAHGU) were enrolled. All four patients are yellow race and underwent diverting ileostomy closure surgery. No other population characteristics would exert potential impact on our analysis.

Recruitment

We recruited four patients who had undergone diverting ileostomy closure surgery at the Second Affiliation Hospital of Zhejiang University (SAHGU). During standard surgery procedure, the surgeon would remove a small portion of rectus abdominis muscle to provide adequate space for tissue reconstruction and achieve optimal stoma retraction. No self-selection bias is present. The muscle debris was collected and minced on ice, and transferred into 10 mL wash medium (WM, Ham's F-10 supplemented with 10% v/v horse serum and 1% penicillin-streptomycin) containing (3825 U/g muscle) collagenase II (Gibco). Tissues were digested in a 37°C shaker for 1 h. The digestion was stopped by adding 40 mL cold WM. Then the cells were centrifuged at 500 g for 5 min at 4°C and the supernatant was aspirated. The pellet was resuspended and digested in WM containing 100 U/mL collagenase II and 1 U/mL dispase II (Gibco) for 30 min at 37°C, then the digestion was stopped as noted above. Cells were then stained and sorted with CD56, CD31, CD45, and CD29 flowcytometry antibodies (CD31-CD45-CD29+CD56+)

Ethics oversight

All procedures involving human samples in this study received ethical approval from the Human Research Ethics Committee of SAHGU (2024-0159). All sample collection is after full informed consent obtained from all four participants.

Note that full information on the approval of the study protocol must also be provided in the manuscript.

Field-specific reporting

Please select the one below that is the best fit for your research. If you are not sure, read the appropriate sections before making your selection.

Life sciences Behavioural & social sciences Ecological, evolutionary & environmental sciences

For a reference copy of the document with all sections, see nature.com/documents/nr-reporting-summary-flat.pdf

Life sciences study design

All studies must disclose on these points even when the disclosure is negative.

Sample size

Sample sizes for all experiments were chosen based on our previous experience (Z Chi, et al. Molecular Cell, 2020; S Chen, et al. Cell metabolism, 2022; C Guo, et al. Immunity, 2018; C Guo, et al. Immunity 2016)

Data exclusions

Low quality cells were excluded for scRNAseq analysis. No data were excluded from the showed experiments.

Replication

A representative or a pool of at least two independent experiments showing similar results have been conducted. And all attempts at replication were reproducibility.

Randomization

All sample involved were allocated into experimental groups randomly.

Blinding

The investigators were not blinded to group allocation during collection and analysis. The approach is considered standard for experiments of the type performed in this study, as the genetic background of mice must be predetermined prior to analysis. For cell experiments, the genetic background and treatment of the cells must be predetermined prior to analysis.

Reporting for specific materials, systems and methods

We require information from authors about some types of materials, experimental systems and methods used in many studies. Here, indicate whether each material, system or method listed is relevant to your study. If you are not sure if a list item applies to your research, read the appropriate section before selecting a response.

Materials & experimental systems

n/a	Involved in the study
<input type="checkbox"/>	<input checked="" type="checkbox"/> Antibodies
<input type="checkbox"/>	<input checked="" type="checkbox"/> Eukaryotic cell lines
<input checked="" type="checkbox"/>	<input type="checkbox"/> Palaeontology and archaeology
<input type="checkbox"/>	<input checked="" type="checkbox"/> Animals and other organisms
<input checked="" type="checkbox"/>	<input type="checkbox"/> Clinical data
<input checked="" type="checkbox"/>	<input type="checkbox"/> Dual use research of concern
<input checked="" type="checkbox"/>	<input type="checkbox"/> Plants

Methods

n/a	Involved in the study
<input checked="" type="checkbox"/>	<input type="checkbox"/> ChIP-seq
<input type="checkbox"/>	<input checked="" type="checkbox"/> Flow cytometry
<input checked="" type="checkbox"/>	<input type="checkbox"/> MRI-based neuroimaging

Antibodies

Antibodies used

Western blot: GSDMD (ab219800, 1:1000, Abcam), Vinculin (db11158, 1:1000, Diagbio), EPHX2 (10833-1-AP, 1:1000, Proteintech), Phospho-p38 MAPK (Thr180/Tyr182) (#4511, 1:1000, CST), p38 MAPK (#8690, 1:1000, CST), Phospho-p44/42 MAPK (Erk1/2) (Thr202/Tyr204) (#4370, 1:1000, CST), p44/42 MAPK (Erk1/2) (#4695, 1:1000, CST), Phospho-Akt (Ser473) (#4060, 1:1000, CST), Akt (#9272, 1:1000, CST), FGF Receptor 1 (#9740, 1:1000, CST), Phospho-4E-BP1 (Thr37/46) (#2855, 1:1000, CST), Ninjurin-1 (sc-136295, 1:1000, Santa cruz), Phospho-p70 S6 Kinase (Thr389) (#9205, 1:1000, CST), eIF4EBP1 (A23500, 1:1000, Abclonal), p70 S6 Kinase 1 (A2190, 1:1000, Abclonal), Phospho-FGFR1-Y653/Y654 (AP1317, 1:1000, Abclonal), EGF Receptor (4267, 1:1000, CST), EGFR (phospho Y1068) (ab40815, 1:1000, Abcam), HMGB1 (ab79823, 1:1000, abcam), Lamin B1 (db13332, 1:1000, Diagbio), VDAC2 (55261-1-AP, 1:1000, proteintech), TOMM20 (11802-1-AP, 1:1000, proteintech), LAMP1 (ab208943, 1:1000, abcam), GM130 (11308-1-AP, 1:1000, proteintech), Calnexin (ab22595, 1:1000, abcam), Goat Anti Rabbit IgG (H+L)-HRP (db10002, 1:5000, Diagbio), Goat Anti Mouse IgG (H+L)-HRP (db10003, 1:5000, Diagbio).
 Immunofluorescence: PAX7 (PAX7, 1:200, DSHB), MYOD (sc-32758, 1:200, Santa cruz), myogenin (F5D, 1:200, DSHB), Ki-67 Monoclonal Antibody (Ki-67), Alexa Fluor™ 647 (MA5-44140, 1:200, Invitrogen), Alexa Fluor® 488 Anti-Ki67 antibody [SP6] (ab281847, 1:200, Abcam), Myosin heavy chain (embryonic) (F1.652, 1:20, DSHB), F4/80 (70076S, 1:200, CST), CD31 (ab222783, 1:200, Abcam), Laminin (L9393, 1:500, Sigma-Aldrich), Cytokeratin 14 (db2817, 1:200, Diagbio), Goat Anti-Rabbit IgG H&L (Alexa Fluor® 488) (ab150077, 1:500, Abcam), Goat Anti-Rabbit IgG H&L (Alexa Fluor® 555) (ab150078, 1:500, Abcam), Goat Anti-Rabbit IgG H&L (Alexa Fluor® 647) (ab150079, 1:500, Abcam), Goat Anti-Mouse IgG H&L (Alexa Fluor® 555) (ab150114, 1:500, Abcam), DAPI solution (C0060, 1:1000, Solarbio), Alexa Fluor™ 660 Ki-67 Monoclonal Antibody (606-5698-82, SolA15, 1:200, Thermo Fisher), AffiniPure Fab fragment goat anti-mouse IgG (115-007-003, 1:100, Jackson).
 FACS: Zombie Aqua™ Fixable Viability Kit (423102, N/A, 1/1000, Biolegend), APC anti-human CD45 Antibody (304011, HI30, 1/500, Biolegend), PE/Cyanine7 anti-human CD31 Antibody (303117, WM59, 1/500, Biolegend), Biotin anti-human CD56 (NCAM) Antibody (318319, HCD56, 1/200, Biolegend), Alexa Fluor® 488 anti-human CD29 Antibody (303015, TS2/16, 1/200, Biolegend), Biotin anti-mouse CD106 Antibody (105704, 429 (MVCA.M.A), 1/200, Biolegend), PE/Cyanine7 anti-mouse Ly-6A/E (Sca-1) Antibody (108113, D7, 1/500, Biolegend), FITC anti-mouse CD31 Antibody (102405, 390, 1/500, Biolegend), FITC anti-mouse CD45 Antibody (157213, S18009F, 1/500, Biolegend), PE Streptavidin (405203, N/A, 1/500, Biolegend), eBioscience™ Streptavidin-APC (17-4317-82, N/A, 1/500, Thermo Fisher), Brilliant Violet 785™ anti-mouse Ly-6C Antibody (128041, HK1.4, 1/500, Biolegend), Brilliant Violet 650™ anti-mouse/human CD11b Antibody (101259, M1/70, 1/500, Biolegend), FITC anti-mouse Ly-6G Antibody (127606, 1A8, 1/500, Biolegend), Brilliant Violet 421™ anti-mouse F4/80 Antibody (123132, BM8, 1/500, Biolegend), APC anti-mouse CD45 Antibody (103112, 30-F11, 1/500, Biolegend), eBioscience™ APC Ki-67 Monoclonal Antibody (17-5698-82, SolA15, 1/200, Thermo Fisher), eBioscience™ PE-eFluor™ 610 Ki-67 Monoclonal Antibody (61-5698-82, SolA15, 1/200, Thermo Fisher).

Validation

We selected them based on cross-reactivity with mouse and human (depending on our research needs) and carefully evaluated the validation data provided by both the manufacturers and literature. In several instances, we performed further validation of antibodies by examining the molecular weight of the band by Western blotting and Knocking out protein of interest. Antibodies were aliquoted and stored as recommended by the manufacturer to minimize freeze thaw cycles and associated loss in performance.

Eukaryotic cell lines

Policy information about [cell lines and Sex and Gender in Research](#)

Cell line source(s)

NIH/3T3 and C2C12 cell lines were from the American Type Culture Collection

Authentication

These cell lines used were originally obtained from ATCC and authenticated by ATCC and our lab using morphology.

Mycoplasma contamination

All cell lines used have been regularly tested to be free of Mycoplasma contamination.

Commonly misidentified lines (See [ICLAC](#) register)

No commonly misidentified cell lines were used.

Animals and other research organisms

Policy information about [studies involving animals; ARRIVE guidelines](#) recommended for reporting animal research, and [Sex and Gender in Research](#)

Laboratory animals

C57BL/6J mice, GsdmdKO, Gsdmd-flo, and Ephx2-flo mice were purchased from Gempharmatech. Lyz2-Cre mice were purchased from the Jackson Laboratory. Gsdmdf/f and Ephx2f/f mice were crossed with Lyz2-Cre mice to obtain Gsdmdf/f-Lyz2-Cre and Ephx2f/f-Lyz2-Cre mice. GsdmdKO mice and their littermate controls were only used for in vitro macrophage experiments unless otherwise

stated. All mice used in experiments were on a C57BL/6 background between 8 and 12 weeks old, while 18 months old mice were used for the aging experiments. The mice were bred in a specific pathogen-free facility in the Laboratory Animal Center of Zhejiang University in accordance with the National Institute of Health Guide for the Care and Use of Laboratory Animals.

Wild animals	The study did not involve wild animals.
Reporting on sex	Mice of both sexes were used throughout the study; sex-matched and age-matched controls were used in individual experiments.
Field-collected samples	The study did not involve samples collected from the field.
Ethics oversight	The mice were bred in a specific pathogen-free facility in the Laboratory Animal Center of Zhejiang University in accordance with the National Institute of Health Guide for the Care and Use of Laboratory Animals. The animal experimental protocols were approved by the Review Committee of Zhejiang University School of Medicine (ZJU20230356) and were in compliance with institutional guidelines.

Note that full information on the approval of the study protocol must also be provided in the manuscript.

Plants

Seed stocks	N/A
Novel plant genotypes	N/A
Authentication	N/A

Flow Cytometry

Plots

Confirm that:

- The axis labels state the marker and fluorochrome used (e.g. CD4-FITC).
- The axis scales are clearly visible. Include numbers along axes only for bottom left plot of group (a 'group' is an analysis of identical markers).
- All plots are contour plots with outliers or pseudocolor plots.
- A numerical value for number of cells or percentage (with statistics) is provided.

Methodology

Sample preparation	Briefly, the hind limb muscles were detached, minced on ice, and transferred into 10 mL wash medium (WM, Ham's F-10 supplemented with 10% v/v horse serum and 1% penicillin-streptomycin) containing 800 U/mL collagenase II (Gibco). Tissues were digested in a 37°C shaker for 1 h. The digestion was stopped by adding 40 mL cold WM. Then the cells were centrifuged at 500 g for 5 min at 4°C and the supernatant was aspirated. The pellet was resuspended and digested in WM containing 100 U/mL collagenase II and 1 U/mL dispase II (Yeasen Biotechnology) for 30 min at 37°C, then the digestion was stopped as noted above.
Instrument	ACEA NovoCyte TM, BD Fortessa, Beckman moflo Astrios EQ.
Software	NovoExpress version 1.5.6, BD FACSDiva™ Software and Summit version 5.0 were used for flow cytometry data acquisition and sorting. FlowJo V10 for FACS results.
Cell population abundance	The purities of the sorted cells were more than 90%.
Gating strategy	For all experiments, FSC-H vs. SSC-H gates was used to identify population targeted viable cells. Singlet cells were separated from doublets using FSC-A vs. FSC-H gates. Live viability dye was used to eliminate dead cells. Target populations were further determined by specific antibodies, which were able to distinguish from negative populations.

Tick this box to confirm that a figure exemplifying the gating strategy is provided in the Supplementary Information.